J. Fluid Mech. (2024), *vol*. 999, A50, doi:10.1017/jfm.2024.896

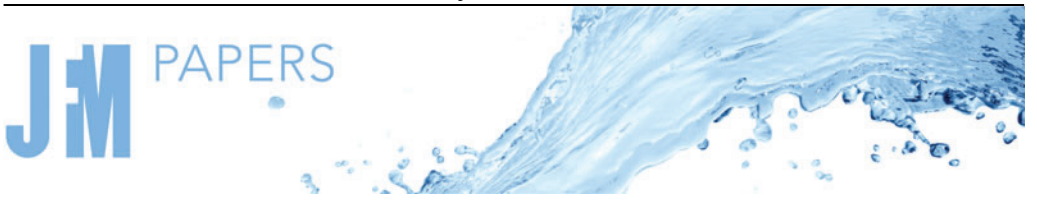

New understanding of the regimes and controlling mechanisms in a falling curtain of particles

Xiaopeng Bi[1,2,†], **Timothy C.W. Lau**[1,3], **Zhiwei Sun**[1,2] **and Graham J. Nathan**[1,2]

[1]Centre for Energy Technology, The University of Adelaide, Adelaide, SA 5005, Australia

[2]School of Electrical and Mechanical Engineering, The University of Adelaide, Adelaide, SA 5005, Australia

[3]UniSA STEM, The University of South Australia, Mawson Lakes, SA 5095, Australia

(Received 15 May 2024; revised 4 September 2024; accepted 9 September 2024)

A stream of free-falling particles from a rectangular hopper, hereafter called a 'curtain', was characterised systematically using a well-resolved, non-intrusive optical shadowgraphic method, to reveal both an additional axial region and an additional dilute region distributed laterally on either side of the curtain, relative to those identified previously. The effects of particle size and hopper outlet thickness on the evolution of the particle curtain were separately isolated, whilst measuring particle mass flow rate. The curtains were characterised into four distinct axial regions, namely a near-field expansion region near to the hopper exit, a neck zone where the curtain contracts, a region of intermediate-field expansion and a far field with particles reaching terminal velocity. The initial expansion half-angle, $2.3^\circ \leq \alpha \leq 4.8^\circ$, was found to be insensitive to particle size, but to increase with hopper outlet thickness. The 'trough' in the neck zone was deduced to be caused by a pressure gradient driven by particle acceleration. The curtain expansion rate at the intermediate field was found to increase with a decrease in particle size and hopper outlet thickness. The outermost dilute-particle region was deduced to be caused by collisions, induced by gradients in the velocity profile near to the hopper exit. New dimensionless analysis reveals that the dynamics of curtains can be characterised broadly into two regimes, one in which the aerodynamics is dominant and the other where it is weak. Curtain transmittance was found to scale with the Froude number, highlighting the importance of particle momentum.

Key words: particle/fluid flow

† Email address for correspondence: xiaopeng.bi@adelaide.edu.au

1. Introduction

A stream of solid particles falling within a quiescent environment is a fundamental class of two-phase flow whose applications include the mining, agriculture, medical and the chemical industries. Therefore, an improved understanding of the dynamics of this two-phase flow has potential to lead to increased process efficiency, product quality, operational safety and environmental sustainability (Johnson, Nott & Jackson 1990; Liu 2003; Eckhoff 2005; Fitzpatrick & Ahrné 2005; Wypych, Cook & Cooper 2005; Abdul-Wahab 2006; Fabiano *et al.* 2014; Ho 2016; Li *et al.* 2016). In most of these applications, solid particles fall under gravity after being released from either a round- or rectangular-shaped orifice at the outlet of a hopper, in which particles are densely packed. The resulting flow is highly complex, since it starts from the 4-way coupling regime (Balachandar & Eaton 2010) with significant particle–particle and particle–fluid interactions, and becomes progressively more dilute through the entrainment of surrounding fluid into the stream, being driven by particles that accelerate due to gravity. These coupled phenomena result in the flow being prohibitively computationally expensive to model in full detail, and challenging to measure accurately. The challenges also result in a lack of detailed understanding of falling particle streams, which we aim to address in the present paper.

An emerging application of falling particle curtains is a class of concentrated solar thermal (CST) technologies, termed 'falling particle receivers' (FPRs), which is being developed to achieve higher temperatures than is possible with commercially available CST systems that employ molten salt technology (Ho & Iverson 2014). The FPRs employ particles that flow from a hopper through a rectangular orifice to generate a 'curtain' of particles as the primary medium to absorb, transport and store the heat from the concentrated insolation (Ho *et al.* 2014). The high flux solar radiation increases the complexity of these flows through phenomena such as radiation absorption, re-radiation, shadowing and extinction (Evans *et al.* 1987; Khalsa & Ho 2011; Ho & Iverson 2014; Kumar, Kim & Lipiński 2018; Ho *et al.* 2019; Kumar, Lipiński & Kim 2020). However, the details of these mutually interacting phenomena are poorly understood, which contributes to sub-optimal receiver design and operation. Furthermore, technical challenges associated with experimental measurements in densely seeded particle flows, such as propensity of probe damage, signal trapping of optical measurements and light attenuation, limit the availability of data suitable for the validation of computational models. The ensuing paucity of data limits the development of reliable engineering design tools, adding cost to the processes of optimising and up-scaling practical receivers. Therefore, the aim of the present investigation is to meet the need for more detailed data to better characterise free-falling particle streams under a systematically varied range of conditions relevant to practical solar receivers.

The main flow parameters that characterise the performance of FPRs include the particle mass flow rate, the curtain opacity (or transmittance), curtain thickness (including the expansion of the curtain in the direction of the thickness), volume fraction, the velocities of both the fluid and particle phases and the particle emissivity (or absorptivity). Relevant research has been conducted since the 1980s (Martin & Vitko 1982; Falcone, Noring & Hruby 1985; Hruby 1986; Hruby *et al.* 1988; Siegel *et al.* 2007; Kim *et al.* 2009; Kim, Moujaes & Kolb 2010; Ho & Iverson 2014; Ho *et al.* 2014; Ho 2016; Ho *et al.* 2016; Ho 2017; Ho *et al.* 2017; Kumar *et al.* 2018; Ho *et al.* 2019; Mills & Ho 2019; Mills *et al.* 2019; Kumar *et al.* 2020). Note that most studies on curtain transmittance (or opacity) use cold models, that are operated at room temperature. Hruby *et al.* (1988) measured the particle velocity and temperature within a curtain comprising aluminium oxide particles

of ≈650 μm diameter over a falling distance of ≈3 m. Two hopper outlet thicknesses were used, $D = 5.1$ and 6.4 mm, both with the same hopper outlet width-to-thickness aspect ratio of 10:1, resulting in particle mass flow rates, $\dot{m}_p$, of 0.02 and 0.04 kg s^{-1}, respectively. Kim *et al.* (2009) measured particle velocity, curtain thickness, curtain opacity and solid volume fraction also along a ≈3 m falling distance as a function of particle mass flow rates ($0.36\,\mathrm{kg}\,s^{-1} \leq \dot{m}_p \leq 6.69\,\mathrm{kg\,s^{-1}}$) for a particle size of $d_p = 697\,\mu\mathrm{m}$ (noting that particle velocity was also measured for $d_p = 150$, 300 and 1291 μm) using sintered bauxite particles (CARBO HSP). Ho *et al.* (2017) measured the particle mass flow rate, velocity, curtain opacity, curtain thickness and particle volume fraction as a function of D using ceramic CARBO particles of nominal diameter 280 μm within a falling distance of less than 2 m. Since these particles have a very high absorptivity of ≈0.9 (Jeong *et al.* 2021), the role of this parameter was neglected in these studies. Despite their pioneering nature, the previous experimental measurements were only conducted at selected positions within the curtain, so that the details of the flow features of the whole stream are yet to be reported. In addition, neither the effects of particle size nor hopper outlet thickness on the evolution of particle distribution or on the flow dynamics, have yet been quantified.

Particle distributions within a free-falling particle stream affect not only the efficiency of solar receivers in CST applications (Ho 2016; Ho *et al.* 2017), but also impact on the generation of unwanted dust from both the receiver and the upstream particle handling processes (Li *et al.* 2016). Other applications include particle transport and mixing through hopper-like devices, with either rectangular or circular orifices, as well as belt conveyors in which particles fall from one end. The particle dispersion from the exit plane has previously been found to be dependent on the initial distribution of particles within the densely packed hopper (Wardjiman *et al.* 2009) and on the ratio between the particle size and the hopper outlet gap (Wang *et al.* 2020). Previous studies using hopper outlet sizes $4\,\mathrm{mm} \leq D \leq 20\,\mathrm{mm}$ and particle sizes in the range of $40\,\mu\mathrm{m} \lesssim d_p \lesssim 1000\,\mu\mathrm{m}$ have shown that the particle flow expands from the near-exit region as it evolves downstream (Cooper & Arnold 1995; Ogata, Funatsu & Tomita 2001; Prado, Amarouchene & Kellay 2013). However, in one particular study (Prado, Amarouchene & Kellay 2011), with $D = 5.3$ mm and $d_p \approx 159\,\mu\mathrm{m}$, the particle-laden stream was found to contract within the measurement region while in another (Wang *et al.* 2020), with $d_p = 5$ mm, the curtain thickness was found to decrease first before increasing with streamwise distance for cases where $D/d_p > 15$. This latter trend was similarly found in another study (Ansart *et al.* 2011) of the influence of D, but with an additional region identified in the middle of the stream where the flow maintains a relatively constant thickness. The lack of a systematic assessment of the influence of these parameters makes it challenging to explain these apparent inconsistencies in the literature.

Particle dispersion further downstream from the hopper exit has been attributed mostly to air entrainment (Ansart *et al.* 2009; Sun *et al.* 2020*b*), but with apparent conflicting trends. The numerical study from Uchiyama (2004) has found that particle size has almost no influence on the rate of entrainment of ambient air into the particle curtain. In contrast, Ansart *et al.* (2009) deduced from their combined numerical and experimental study that smaller particle sizes can lead to the increase in both the amount of air entrained and the extent of particle dispersed, while Esmaili *et al.* (2015) found the totally opposite trend from their simulations. Additionally, Liu, Cooper & Wypych (2007) ascribed the increase of air entrainment to the large particle size and/or lower particle density in their experiments. However, they did not isolate the relative contribution of these effects. These apparent contradictions about the effect of particle size on the particle distribution within a free-falling particle flow are difficult to explain without sufficient direct experimental measurements as a function of falling distance. Similarly, no systematic study is available

for the influence of the hopper outlet size. These inconsistencies and lack of a sufficiently detailed and systematic data demonstrate the limitations in the current understanding of the complex influences of d_p and D on the particle distribution within falling particle curtains.

Regimes of falling particle streams have been characterised previously based on particle spatial distribution and particle velocity (Wang *et al.* 2016; Sedaghatizadeh *et al.* 2022). Sedaghatizadeh *et al.* (2022) have classified the falling particle stream based on particle velocity into three regimes including the hopper-flow dominant regime, that is, the near-exit region where the flow is most influenced by the hopper, the similarity regime where aerodynamic drag becomes important and the terminal velocity regime, where the particles asymptotically approach their terminal velocity. The latter two regimes are conceptually similar to the 'transitive' and 'dispersive' regimes identified in the experimental work of Wang *et al.* (2016), based on particle distribution. However, there is no clear link between the two systems of characterisations because the influence of hopper outlet geometries has not yet been isolated and there is a lack of understanding of the controlling dimensionless parameters to help bridge the two types of analysis. A stable regime close to the hopper exit has been identified by Wang *et al.* (2016) based on the particle spatial distribution upstream of where a 'rupture' of the particle stream occurs. However, this feature was not reported in the hopper-flow dominant regime identified in the simulations of Sedaghatizadeh *et al.* (2022), who used a different type of hopper, and insufficient experimental data are available to explain these differences. Similar features can also be partially and indirectly found from other falling particle studies but there is a lack of regime quantification (Ogata *et al.* 2001; Ansart *et al.* 2009; Wang *et al.* 2016). Although some studies to characterise the falling particle flow regimes have been conducted, a more detailed experiment is needed with parameters systematically studied to quantify the regimes and provide a more reliable basis for model validation.

In light of the gaps in knowledge identified above, the overall aim of the present study is to provide a much more comprehensive understanding of the effects of particle size and hopper outlet thickness on key aspects of densely seeded falling particle curtains from new measurements at room temperature. In particular, we aim to measure, define and characterise the different flow regimes/regions in the evolution of the particle free-falling process based on prominent flow features, including instantaneously measured particle curtain transmittance and expansion using a spatially resolved, non-intrusive, optical method. We also aim to advance the theoretical understanding of the relationship between these flow characteristics and the resultant mass flux by comparing the data with calculations employing existing analytical models.

2. Approach

2.1. *Experimental set-up*

The experiment consists of measurements of a stream of solid particles falling from a wedged-shape hopper with a rectangular orifice into a quiescent environment, as shown in figure 1. The particles fall under the influence of gravity, forming a pseudo-two-dimensional particle-laden flow downstream from the hopper outlet, which we refer to as the particle 'curtain'. Four different hopper outlet gap thicknesses, $D = 3$, 4, 5 and 8 mm were assessed, with the width of the hoppers fixed at $W = 60$ mm, resulting in a minimum hopper outlet aspect ratio of $W/D = 7.5$. This aspect ratio is sufficiently large for effects from the hopper sidewall to be small (Sun *et al.* 2020*a*). The wall inclination half-angle (relative to the vertical) of the hoppers was selected to be 5° to mitigate the potential 'arching' of particles within the hoppers. This condition results in groups of

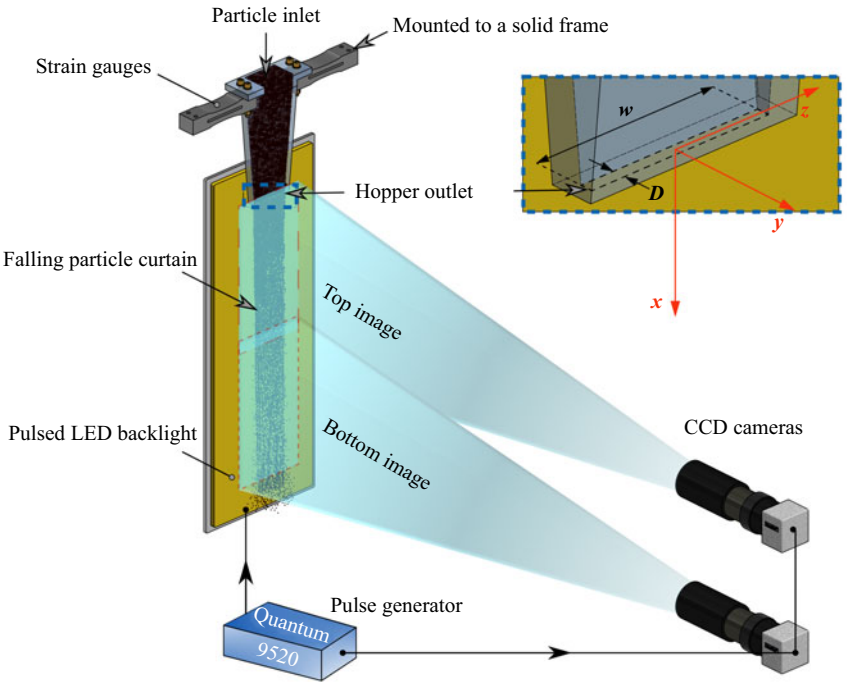

Figure 1. Experimental arrangement used to generate and measure the free-falling particle curtain (not to scale). The two imaging sections have an overlap of ≈10 %. A pulse generator was used to synchronise the LED backlight and CCD cameras. The distance between the hopper centreplane and the backlight was 120 mm, while the origin of the coordinate system corresponds to the centre of the hopper outlet.

particles forming a static 'bridge' from one side of the hopper to the other, inhibiting particles above the 'bridge' from moving through it, thereby reducing the flow rate of particles through the hopper outlet (Nedderman *et al.* 1982; Cleary & Sawley 2002; Anand *et al.* 2008; Datta *et al.* 2008). All four hoppers were manufactured by CNC machining of an aluminium block with a precision of better than 0.1 mm, providing a very smooth and rigid internal wall surface. Particles were discharged by removing a rigid gate (not shown for clarity) positioned ≈1 mm below the hopper outlet to avoid any initial vibration. For all experiments, the ambient air temperature was $22 \pm \approx 2\,^{\circ}\mathrm{C}$ and the relative humidity was kept below 50 %.

The experiments comprise measurements of particle curtain transmittance and curtain thickness utilising a backlighting technique (also known as shadowgraphy), together with particle mass flow measurements. For the backlighting technique, a 257 mm × 1158 mm LED panel was used to generate pulsed, diffuse light with the pulsation frequency and pulse duration fixed at 6.25 Hz and 100 µs, respectively. Images of the backlight penetrating through the particle curtain were measured using two CCD cameras, each equipped with an 80 mm focal length Tamron lens set at an aperture of f/3.8. The two cameras recorded different regions of the flow simultaneously, with the combined imaging region comprising $0 \lesssim x \lesssim 940\,\mathrm{mm}$ and $-60\,\mathrm{mm} \lesssim z \lesssim 60\,\mathrm{mm}$, where x is the axial distance from the hopper outlet plane and z is the coordinate along the width of the hopper, as shown in figure 1. The cameras were synchronised with the pulsed LED panel (i.e. at 6.25 Hz) through a digital delay pulse generator (Quantum 9520 Series), with an exposure time of 100 µs, which is sufficiently short to 'freeze' the image of the flow

Total size of imaging windows (mm)	940 × 120
Overlapping area between cameras (%)	10
LED panel size (mm)	257 × 1158
Distance from backlight to hopper centreplane (mm)	120
Lens	Tamron (f/3.8)
Imaging frequency (Hz)	6.25
Exposure time (μs)	100

Table 1. A summary of the imaging configuration.

(Kim *et al.* 2009). Multiple spirit levels, plumb lines and transparent targets with a grid spacing 3.55 mm grid^{-1} were used to ensure that the hopper exit plane was parallel to the ground, the hopper centreplane was aligned with gravity, and the cameras were mounted perpendicular to the backlight. A summary of the imaging configuration is shown in table 1.

For the curtain transmittance measurements, where the curtain transmittance, T, is defined as the fraction of the incident light that passes through the particle curtain, the hopper was mounted such that the width of the curtain and the imaging plane were co-planar, such that the cameras image the 'front' view of the particle curtain, as shown in figure 1. In this orientation, the backlight panel and the hopper centreplane were co-planar with a fixed distance of 120 mm. This distance is sufficiently large to ensure that any wall effects from the backlight panel on the entrained air flow (e.g. Coanda effect) can be neglected (Sun *et al.* 2020*a*,*b*). For the curtain thickness measurements, the hopper was rotated 90° (about the vertical axis) relative to the hopper orientation in the transmittance measurements, such that the cameras image the 'side' view of the particle curtain. With the pseudo-two-dimensional approach, the effect of the third, spanwise, dimension has been considered in the measurements of curtain transmittance via studies of the effect of hopper outlet thickness (along y-axis). Here, the term 'pseudo' is used because it is impossible to entirely eliminate three-dimensional effects in any nominal two-dimensional configuration, even with a large aspect ratio, as has been previously found in a related investigation by Deo, Mi & Nathan (2007). Nevertheless, the effects of aspect ratio are second order. Therefore, whilst the hopper flows evaluated in our study will differ slightly from those with higher aspect ratios, the dominant physical mechanisms, and hence also the scaling relationship, will still apply. In light of the objective of our study, namely to advance understanding of the scaling relationship, the use of the pseudo-two-dimensional approach is therefore entirely appropriate.

For each flow condition, a minimum of 285 total images of the curtain were recorded for each view. To achieve this number of images, several repetitions of each flow were required, ranging from 3 (for the smallest hopper, where the mass flow rates are low) to 7 (for the largest hopper). At the end of each day, images were also recorded without particles (i.e. the backlight only), with the camera lenses capped (to record the camera dark charge) and with a thin wooden, black, board of approximately the same size as the particle curtain positioned on the hopper centreplane. The latter was used to define a transmittance of zero, noting that the camera intensity never reached zero even after accounting for the dark charge due to stray light from the backlight diffusing off the walls of the laboratory being recorded by the camera. The backlight-only images were used to define complete transmittance (with more details provided in § 2.2). Care was taken to ensure that no pixels were saturated for any of the recorded images.

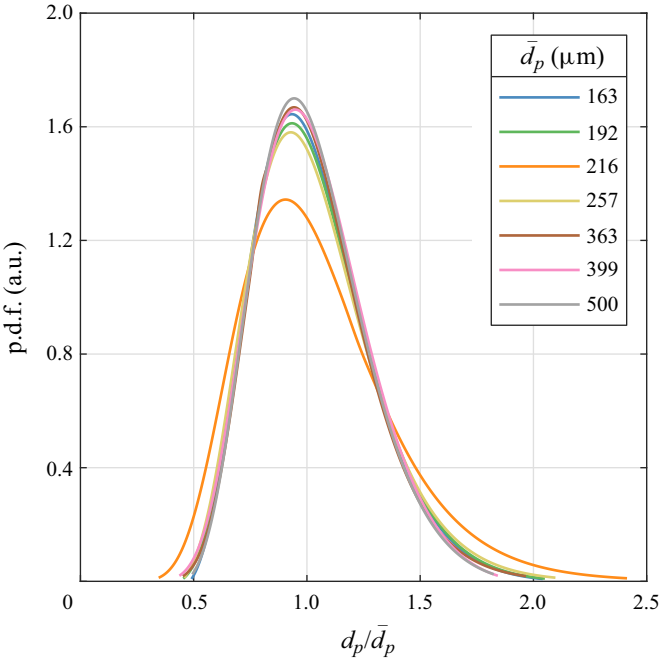

Figure 2. The probability density function (p.d.f.) of particle size, normalised by the measured median particle diameter, $\bar{d}_p$.

Particle mass flow rate measurements were also conducted simultaneously with the particle curtain imaging. This was done using a pair of strain gauges to measure the instantaneous total weight of the hopper and the particles contained within it at a sampling frequency of 1000 Hz. The strain gauges were calibrated with known masses at the beginning of each day. The recorded weight loss of the particles from the hopper was then differentiated with respect to time to provide the instantaneous particle mass flow rate, $\dot{m}_p$. For any flow condition, the mass flow rates were found to be highly repeatable, with the maximum discrepancy between the mass flow rates for the side view and front view (for the same flow condition) less than 2 % (based on one standard deviation about the mean).

The particles used were aluminosilicate ceramic particles (CARBOBEAD CP) with a material density of $\rho_p = 3270\,\mathrm{kg\,m^{-3}}$, a roughness of 0.9 and a sphericity of 0.9 according to the manufacturer's specifications (Carbo Ceramic, Inc. 2022). These particles have been widely employed in studies relevant to solar receivers due to their high solar absorptance and mechanical durability, combined with low cost (Falcone *et al.* 1985; Hruby 1986; Ho *et al.* 2014; Knott *et al.* 2014; Siegel, Gross & Coury 2015; Ho 2016; Ho *et al.* 2017; Kumar *et al.* 2018, 2020; Bagepalli *et al.* 2020; Gobereit *et al.* 2020; Lewis *et al.* 2021, 2022; Ang *et al.* 2022). The low forward scattering and weak wavelength dependent properties (over the range 380 to 1020 nm) of this particle are well suited to the backlighting method, since any light scattering is expected to be negligible (Jeong *et al.* 2021). Seven particle sizes were used, corresponding to particles sieved through seven different US standard mesh sizes. The size distribution of the particles were measured using a particle size analyser (Malvern Mastersizer 2000), with the results (presented in figure 2) showing that the median particle diameters (by volume) for the seven different mesh sizes are $\bar{d}_p = 163$, 192, 216, 257, 363, 399 and 500 μm. A summary of the particle median diameters by

Mesh size	$\bar{d}_p$	$\sigma_p/\bar{d}_p$
70/140	163	24.1 %
50/140	192	24.8 %
40/140	216	32.7 %
40/100	257	26.6 %
40/70	363	25.5 %
30/70	399	24.1 %
30/60	500	23.7 %

Table 2. A summary of the median particle diameter and normalised standard deviation of particle diameter for the seven different mesh sizes used in this study. Here, $\bar{d}_p$ is the median particle diameter by volume (μm), $\sigma_p/\bar{d}_p$ is the normalised standard deviation of particle diameter in percentage.

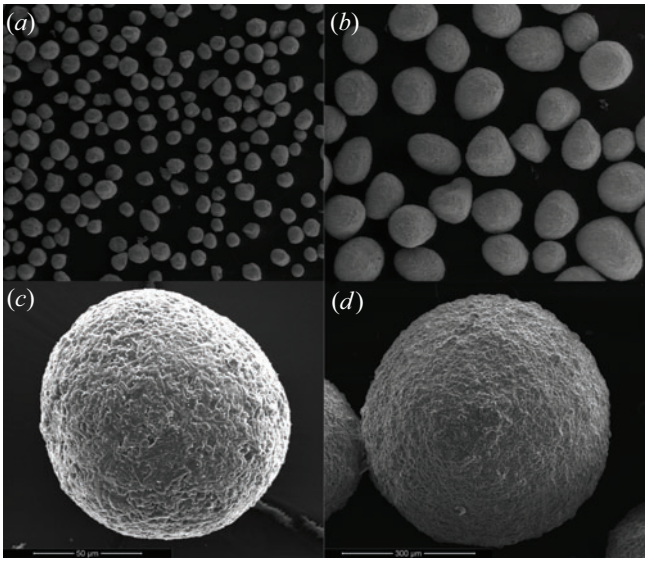

Figure 3. Scanning electron microscopy images of samples of the smallest (163 μm, (*a*,*c*)) and the largest (500 μm, (*b*,*d*)) CARBOBEAD CP ceramic particles used in the present study. The top row comprises a sample of multiple particles, while the bottom row shows zoomed-in images of individual particles (at different scales).

volume, together with one standard deviation of the particle diameter, for all mesh sizes are shown in table 2. As can be seen, the normalised standard deviation of the particle diameter for all seven mesh sizes fall in the range $23.7\,\% \leq \sigma_p/\bar{d}_p \leq 32.7\,\%$. In addition, the dimensionless ratio between particle size and hopper outlet thickness is $\bar{d}_p/D \leq 1/6$, which is sufficiently small to avoid clogging of particles at the hopper exit (Mankoc *et al.* 2007; Janda, Zuriguel & Maza 2012). Figure 3 provides a visual representation of the smallest (163 μm) and the largest (500 μm) particles using scanning electron microscopy images.

The influence of hopper fill height on the particle mass flow rate was found to be negligible in the present experiments for all particle diameters and hopper sizes. This is expected because the friction coefficient between the particles has been identified as having the dominant influence on particle mass flow rates, rather than the particle–wall friction (Anand *et al.* 2008; Bagepalli *et al.* 2020). That is, for these particles, both the

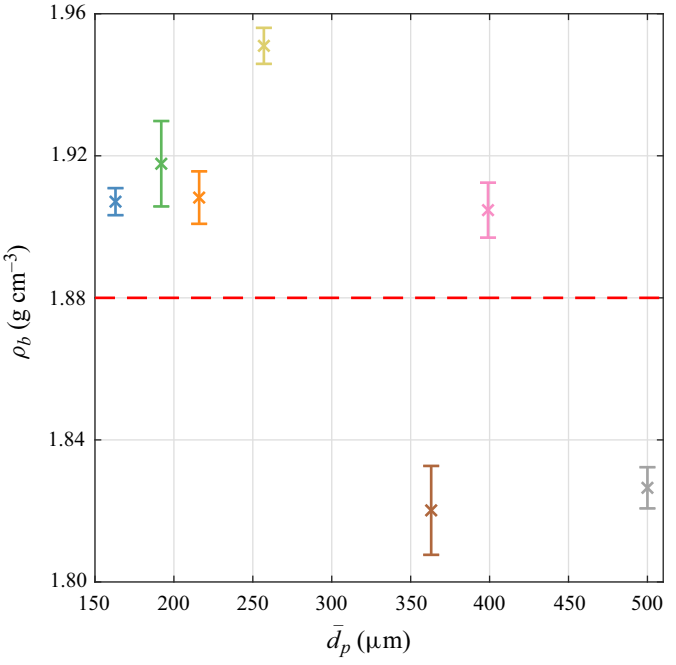

Figure 4. Measured bulk densities of seven different CARBO particle sizes using a graduated 2 litre cylinder. The red dashed line represents the bulk density of 1.88 g cm^{-3} quoted by the manufacturer.

inter-particle sliding friction coefficient of $\mu_s = 0.51$ and the rolling friction coefficient of $\mu_r = 0.37$ measured previously were found to exceed the reported critical threshold of the particle–particle friction coefficient, $\mu_s = 0.2$ (Anand *et al.* 2008; Bagepalli *et al.* 2020).

The particle bulk density, ρ_b, was measured for the 7 different particle sizes utilising a high accuracy weighing scale and a 2 litre graduated cylinder. Each measurement was repeated 5 times. The mean and standard deviation (the latter shown as error bars) of the particle bulk density are presented in figure 4. The maximum standard deviation in the bulk density measurement was 0.69 %. The bulk densities of the particles exhibit up to a 4 % difference compared with the manufacturer's quoted bulk density of 1.88 g cm^{-3} (regardless of particle size), as shown in figure 4. Interestingly, the bulk densities of the 363 and 500 μm particles are below the manufacturer's specifications, while for the other five particle sizes, the bulk densities are greater. A potential reason for this may include slight differences in particle shape for the different particle sizes.

2.2. *Data processing*

The particle curtain transmittance, $T = I/I_0$ where I_0 and I are the incident and transmitted light intensity (or irradiation), respectively, was derived based on the front view measurements utilising the formula $T = (J_{curt} - \bar{J}_{BB})/(\bar{J}_{BL} - \bar{J}_{BB})$, where J is the measured image pixel intensity, while the subscripts 'curt', 'BL' and 'BB' refer to the cases where images of the particle-laden curtain flow, the backlight only and the black board were taken. Here, the overbar denotes time-averaged measurements. The calculation of T was done on a pixel-by-pixel basis for each instantaneous image of the particle-laden flow (i.e. the curtain). The average transmittance at any given height was calculated by spatially averaging the transmittance at each height in the range $-15\,\text{mm} < z < 15\,\text{mm}$.

Note that, since the width of the curtain is 60 mm (i.e. in the range $-30\,\text{mm} \leqslant z \leqslant 30\,\text{mm}$), the average transmittance at any given height is only based on the central portion of the curtain (i.e. excluding data near to the curtain edges). Opacity can be then calculated via $Op = 1 - T$.

The particle curtain thickness was quantified based on the side-view measurements at each streamwise distance using the full width at half-maximum of the lateral opacity distribution, $\Delta_{0.5}$. That is, the curtain thickness is the lateral extent between the locations where the opacity is 50 % of the peak opacity, outlining the dense core of the particle curtain, which is consistent with previous studies (Kim *et al.* 2009; Ho *et al.* 2017). A dilute-particle region surrounding the curtain core was also quantified by its thickness, as characterised by the lateral distance between the half-width ($\Delta_{0.5}$) and the location of 5 % of the peak opacity ($\Delta_{0.05}$).

Images where the flow was clearly not at steady state (e.g. the first and last few frames of the particle-laden flow) were removed from the analysis. Images from the two cameras were aligned to within $\approx \pm 1$ pixel using the images of the targets. Further image alignment with sub-pixel accuracy was obtained by cross-correlation of the region where two instantaneous images overlapped, and computing the time-averaged displacement between the two overlapping regions.

3. Analytical models

Insights into the particle dynamics of free-falling particle curtains were obtained from analytical methods based on the equations of motion for falling particles under simplified conditions. These models assume single, spherical particles falling under the influence of gravity in a quiescent environment. The interactions of the particles with the fluid are considered under two extreme scenarios, namely (a) a zero-drag scenario, representing the case where the entrained fluid velocity is equal to the particle velocity (i.e. the particle slip velocity is zero), and (b) the Stokes regime, where the drag on the particle is described by Stokes law. The former and latter scenarios are expected to represent the lower and upper bounds of particle drag, respectively. Under these conditions, a force balance on the particle results in

$$\frac{\partial U_p}{\partial t} = g - \frac{F_D}{m_p}, \tag{3.1}$$

where g is the gravitational acceleration, U_p is the particle velocity in the axial direction, F_D is the drag force on the particle in the upward axial direction and m_p is the mass of a single particle.

3.1. *Equations of motion for the zero-drag scenario*

For the scenario where the particles are subject to zero drag (i.e. $F_D = 0$), the particle velocity ($U_{p,ZD}$) is thus derived directly from the integration of (3.1), as described by the following equation:

$$U_{p,ZD}(x) = (U_0^2 + 2gx)^{1/2}, \tag{3.2}$$

where $U_{p,ZD}$ is the particle velocity in the axial direction for the zero-drag scenario, U_0 is the particle initial velocity in the axial direction near to the hopper exit and x is the vertical distance from the hopper exit (figure 1).

3.2. *Equations of motion for the Stokes regime*

For the case where the particle Reynolds number is very small (i.e. the Stokes regime), the drag on the particle can be described by $F_D = 3\pi\mu d_p U_s$, where μ is the dynamic viscosity of the fluid and U_s is the particle slip velocity. Using (3.1), and assuming that the fluid phase axial velocity, U_f, is constant throughout the flow, the particle velocity is then

$$U_{p,SD}(t) = U_{t,SD}\left[1 - \exp\left(-\frac{t}{\tau_p}\right)\right] + U_0 \exp\left(-\frac{t}{\tau_p}\right), \tag{3.3}$$

where $U_{t,SD} = \tau_p g - U_f$ is the particle terminal velocity (U_f represents the upward fluid motion; hence, the negative sign is used here), t is time, $\tau_p = (\rho_p d_p^2)/(18\mu)$ is the particle time scale and ρ_p is the particle material density. Here, the subscript 'SD' stands for Stokes drag. Using the chain rule, the particle velocity can also be expressed in terms of the falling distance, i.e.

$$U_{p,SD}(x) = W\left[\left(\frac{U_0}{U_{t,SD}} - 1\right)\exp\left(\frac{U_0}{U_{t,SD}} - 1\right)\exp\left(-\frac{x}{U_{t,SD}\tau_p}\right)\right]U_{t,SD} + U_{t,SD}, \tag{3.4}$$

where the symbol 'W' denotes the principal branch of the Lambert W function. The particle acceleration as a function of axial distance can then be expressed as follows:

$$a_{p,SD}(x) = \frac{U_{t,SD} - U_{p,SD}(x)}{\tau_p}. \tag{3.5}$$

3.3. *Curtain light transmittance model*

A simplified model for the transmittance through a particle curtain can be obtained by invoking the Beer–Lambert law, i.e.

$$T = \exp[-\sigma\bar{\theta}(x)\Delta(x)], \tag{3.6}$$

where σ is the absorption cross section of the particles and $\bar{\theta}(x)$ and $\Delta(x)$ are the average particle number density and the thickness of the particle curtain at the given falling distance, respectively. The overbar indicates the value averaged over the curtain width.

The particle mass flow rate at any given height can be calculated from

$$\dot{m}_p = \rho_p \forall_p \int_0^A \theta U_p \,\mathrm{d}A, \tag{3.7}$$

where A is the cross-sectional area of the particle curtain, $\forall_p$ is the volume of a single particle and θ is the local particle number density. Assuming that the particle number density and velocity are approximately uniform across the lateral plane at any given distance from the hopper exit, then the particle mass flow rate per unit width can be expressed as

$$\dot{M}_p = \rho_p \forall_p \bar{\theta}(x)\bar{U}_p(x)\Delta(x). \tag{3.8}$$

Combining this (3.8) with (3.6), and assuming that the absorption cross-section for the current particles can be approximated by their cross-sectional areas, we obtain

$$T(x) = \exp\left[-\frac{3\dot{M}_p}{2\rho_p d_p \bar{U}_p(x)}\right]. \tag{3.9}$$

Therefore, the analytical transmittance can be predicted with either the zero-drag model or in the Stokes regime. This involves replacing $\bar{U}_p$ in (3.9) with $U_{p,ZD}$ or $U_{p,SD}$, respectively.

Importantly, (3.9), together with (3.2) or (3.4), provides an analytical model of the axial evolution of the particle curtain transmittance based on the particle properties, particle mass flow rate and hopper outlet thickness. This model can be used to provide a first-order estimate of curtain transmittance, while also providing an analytical base in which to interpret the measured results, as discussed in § 4.4.

4. Results and discussion

4.1. *Particle mass flow rates*

The particle mass flow rate for particles exiting a hopper can be estimated from the well-established Beverloo equation (Beverloo, Leniger & Van de Velde 1961), given by

$$\dot{M}_p = C_1 \rho_b g^{0.5} D_{eff}^{1.5}, \tag{4.1}$$

where $D_{eff} = D - C_2 \bar{d}_p$ is the effective hopper outlet thickness, which takes into account the influence of a thin layer of slow (or non-) moving particles near to the wall of the hopper exit, resulting in a reduction in the effective hopper outlet size (Beverloo *et al.* 1961; Mankoc *et al.* 2007; Janda *et al.* 2012). The degree to which the effective hopper outlet size is reduced by the presence of particles is taken into account through the coefficient C_2, which is likely influenced by the particle and hopper surface properties (Beverloo *et al.* 1961; Mankoc *et al.* 2007). The coefficient C_1 in (4.1) is a lumped parameter which partially takes into account the flow resistance due to particle–particle and particle–wall friction, with the value of C_1 expected to be approximately inversely proportional to the friction within the flow.

Re-arranging (4.1) results in the normalised particle mass flow rate per metre of hopper width as follows:

$$\tilde{m} = \frac{\dot{M}_p}{\rho_b g^{0.5} D^{1.5}} = C_1 \left(1 - \frac{C_2 \bar{d}_p}{D}\right)^{1.5}. \tag{4.2}$$

Since C_1 may be influenced by particle size, (4.2) can be fitted for any given particle size with the measured experimental data to obtain C_1 as a function of the reciprocal of particle diameter, $1/\bar{d}_p$. The results are presented in figure 5(*a*). These show that the value of C_1 is approximately linearly proportional to the reciprocal of particle diameter, increasing with $\bar{d}_p$. Since $\tilde{m}$ is linearly proportional to C_1, this implies that, all else being equal, the particle mass flow rate will increase with $\bar{d}_p$. This is attributed to the decrease in surface area (per unit volume) as $\bar{d}_p$ is increased, which in turn reduces particle–particle friction. A linear curve fit of the data in figure 5(*a*) results in $C_1 \approx -0.0416/\bar{d}_p + 1.91$ (note that the first coefficient on the right-hand side of the equation has dimensions of mm), which suggests that, for the cases where the particles are large, $C_1 \to 1.9$. Nevertheless, the values of $1.63 \leq C_1 \leq 1.84$ found here are significantly different from the $C_1 = 1.033$ obtained by Kim *et al.* (2009) and Ho *et al.* (2017) using similar particles, and from the value of $C_1 = 0.583$ measured by Beverloo *et al.* (1961) using agricultural solids. The higher value of C_1 found in the present experiment is attributed to differences in hopper angle. For example, the present experiment utilises wedged-shaped hoppers with a wall inclination half-angle of 5°, while the hoppers used in Beverloo *et al.* (1961), Kim *et al.* (2009) and Ho *et al.* (2017) had the opening on a flat bottom, with a hopper wall inclination half-angle of 90°. It is known from the previous studies that a smaller hopper angle leads to an increase in the particle mass flow rates (Brown 1961; Anand *et al.* 2008). Taking the effect of hopper

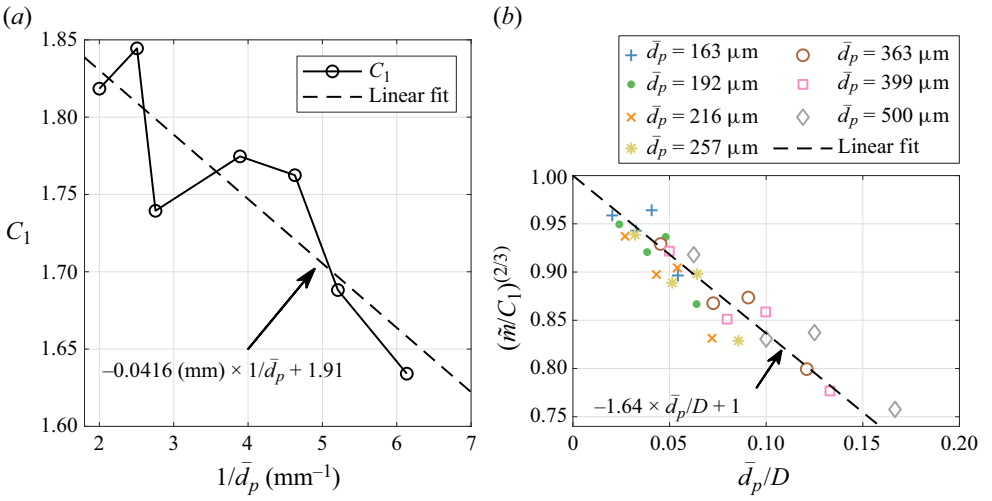

Figure 5. The variation of the parameter C_1 as a function of the inverse of particle diameter, together with the measured mass flow rate parameter $(\tilde{m}/C_1)^{2/3}$ as a function of normalised particle size. Here, C_1 and $\tilde{m}$ are from (4.2). The black dashed line in both figures represents a linear curve fit of the data.

angle into account, a greater value of C_1 found in the present measurements is therefore consistent with previous work.

Figure 5(*b*) presents the term $(\tilde{m}/C_1)^{2/3}$ as a function of the normalised particle diameter, $\bar{d}_p/D$, for all investigated hopper sizes and particle diameters. The axes in this figure were chosen on the basis that the data should follow a linear profile according to (4.2). The results show that the data for all particle diameters and hopper sizes collapse onto a single linear profile. A linear curve fit of the data results in a profile following the formula $(\tilde{m}/C_1)^{2/3} = 1 - 1.64\bar{d}_p/D$. That is, the value of C_2 found in the present experiments is approximately constant at $C_2 = 1.64$. The constant C_2 is slightly higher than the value 1.4 reported by Beverloo *et al.* (1961), Kim *et al.* (2009) and Ho *et al.* (2017). The reason for this small discrepancy is unclear, although it could be due to differences in the particle properties (e.g. the particle–particle friction) between the present experiments and the previous studies. Nevertheless, the results show that with a constant value of C_2, and with C_1 varying with $\bar{d}_p$ according to figure 5(*a*), the measured mass flow rates are close to that estimated from the linear curve fit formula to within 5.8 %. This result provides evidence that C_1 is highly dependent on particle size, while C_2 is relatively insensitive to particle size, for any given particle type.

The results presented here also demonstrate that the Beverloo equation particularly suits the scaling assessments of flows in a hopper because it is an analytical equation that directly accounts for the dominant dimensionless parameters, whilst lumping the second-order terms to incorporate, albeit imperfectly, the influence of highly complex and nonlinear processes, into the two empirical parameters C_1 and C_2. These parameters simplify with reasonable accuracy the complex particle dynamics in the granular (highly dense) flow regime inside the hopper and include the influences of particle size distribution, surface roughness and shape on the particle–particle and particle–wall interactions. The challenges of advancing the understanding in this environment mean that, despite many attempts to improve on it for specific scenarios, no widely acknowledged method has yet emerged.

4.2. *Particle curtain expansion*

Figure 6 presents a representative instantaneous image of the side view of the free-falling particle curtain. As can be seen, the particle curtain thickness is small relative to its streamwise length, with the particles falling predominantly in the direction of gravity, consistent with previous work (Ho *et al.* 2017). Visual inspection of the particle curtain flow also reveals that there are three distinct flow regions which characterise the particle curtain flow in the direction of particle fall, namely a near-field expansion, a neck zone and an intermediate-field expansion. The 'near-field expansion' occurs near to the hopper exit (i.e. approximately within the first few hopper outlet thicknesses from the exit), and is characterised by strong particle dispersion laterally from the centreline, as can be seen from the zoomed-in inset on the right-hand side of figure 6. Downstream from the near-field expansion region, the particle curtain appears to reduce in thickness with streamwise distance. This region is called the 'neck zone', and may extend as far downstream as $x/D \approx 100$. Further downstream from this neck zone, the curtain can be seen to expand again with downstream distance. In this 'intermediate-field expansion', the curtain can be seen to exhibit large-scale flow unsteadiness that spans the entire width of the curtain. This unsteadiness is consistent with previous work, being driven by the shear force between the curtain and the surrounding flow, which generates such roll-up features (Möbius 2006; Amarouchene, Boudet & Kellay 2008; Lau & Nathan 2016; Chu *et al.* 2020). It should be noted that the term 'intermediate field' is used here, as distinct from the more commonly used 'far field', because the latter typically refers to the region of the flow where particles approach their settling velocity (Sedaghatizadeh *et al.* 2022), which is not necessarily true in the present intermediate field.

Visualisation of the particle curtain flow also shows that the lateral distribution of particles can be characterised by a local 'core' region of densely seeded particles close to the centreline where the flow opacity approaches unity (the black regions in the figure), whose position fluctuates with time in the downstream region of the curtain. Surrounding this 'core' region, a dilute-particle region can be seen where the opacity is noticeably lower than unity. From a practical perspective, the lateral dispersion of particles away from the main curtain is also important, since it is likely to be a key contributor to the generation of 'dust' that has potential to escape from devices such as FPRs to generate both a challenge to reduce pollution and a loss of efficiency.

Figure 7 presents instantaneous side-view images of the particle curtain issuing from a single hopper for seven different particle sizes. Here, the hopper outlet thickness is fixed at $D = 5$ mm. The three particle curtain regions can be generally identified for all particle sizes. The largest particle size can be seen to exhibit the overall greatest curtain thickness in the upper half of the curtain. However, the flow features including the neck zone and the unsteady fluctuation of the curtain in the intermediate field become more prominent with a decrease in particle size. Particles with different size distributions, shapes (e.g. oval or cylindrical) and surface roughnesses will inevitably influence the particle flow behaviour via particle–wall, particle–particle and particle–fluid interactions, causing differences in the values. However, the controlling scaling relationship will still apply, albeit with somewhat different values.

Figure 8 presents the time-averaged measurements of the axial evolution of the particle curtain thickness ($\Delta_{0.5}$) as a function of falling distance for seven particle sizes ($\bar{d}_p =$ 163, 192, 216, 257, 363, 399 and 500 μm) and for two hopper outlet thicknesses ($D = 3$ and 8 mm). Note that reliable data are not available immediately below the hopper exit, $0 \leq x/D \lesssim 1$, due to the parallax error, i.e. the edge of the hopper closer to the backlight obscures light through a small region of the flow in front of it near to the exit. Nevertheless,

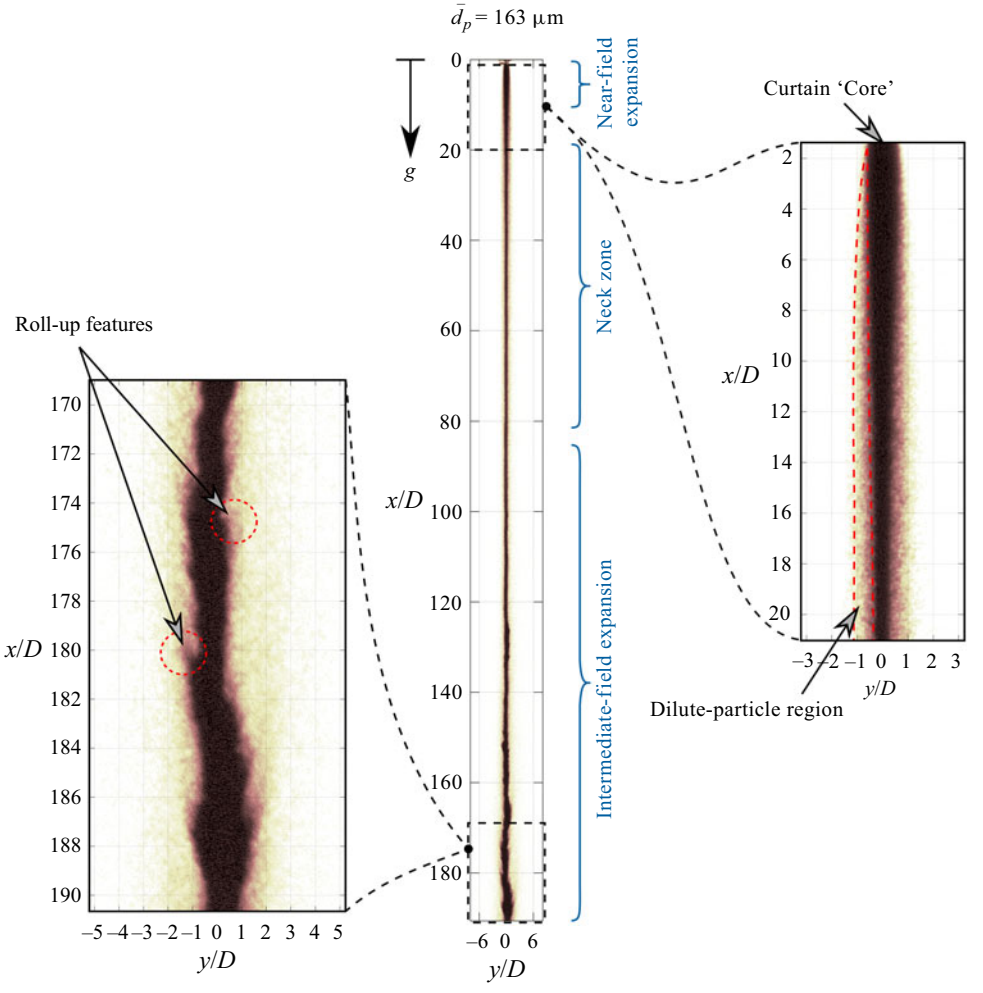

Figure 6. An instantaneous side-view image of the particle curtain, with an illustration of the three characteristic regions of the falling particle curtain, namely the near field, the neck zone and the intermediate field. In this case, $D = 5$ mm and $\bar{d}_p = 163\,\mu$m. Also shown is the dilute-particle region where particles at the edge of the curtain interact with the surrounding flow, resulting in a region of low particle volume fraction relative to the core of the curtain.

the results show that, for all of these particles and hopper outlet thicknesses, there is a strong increase in $\Delta_{0.5}$ with downstream distance in the near-field expansion region ($0 \lesssim x \lesssim 75$ mm), due to strong particle dispersion away from the centreline, consistent with the results presented in figure 6. The presence of this near-field expansion was also observed in similar studies of particles falling from a round hopper with $4\,\text{mm} \leq D \leq 20\,\text{mm}$ and $40\,\mu\text{m} \lesssim d_p \lesssim 1000\,\mu\text{m}$ (Cooper & Arnold 1995; Ogata *et al.* 2001; Prado *et al.* 2013). The reason for this phenomenon is yet to be confirmed, but we postulate that it is due to particle collisions near to the hopper exit. More specifically, particle dispersion away from the centreline could be attributed to collisions between the faster moving particles near to the hopper centreline and the slower moving particles near to the hopper wall.

Interestingly, the initial rate of expansion (i.e. the gradient of the curves in figure 8) in the near field is approximately the same for all particle sizes and for any given hopper

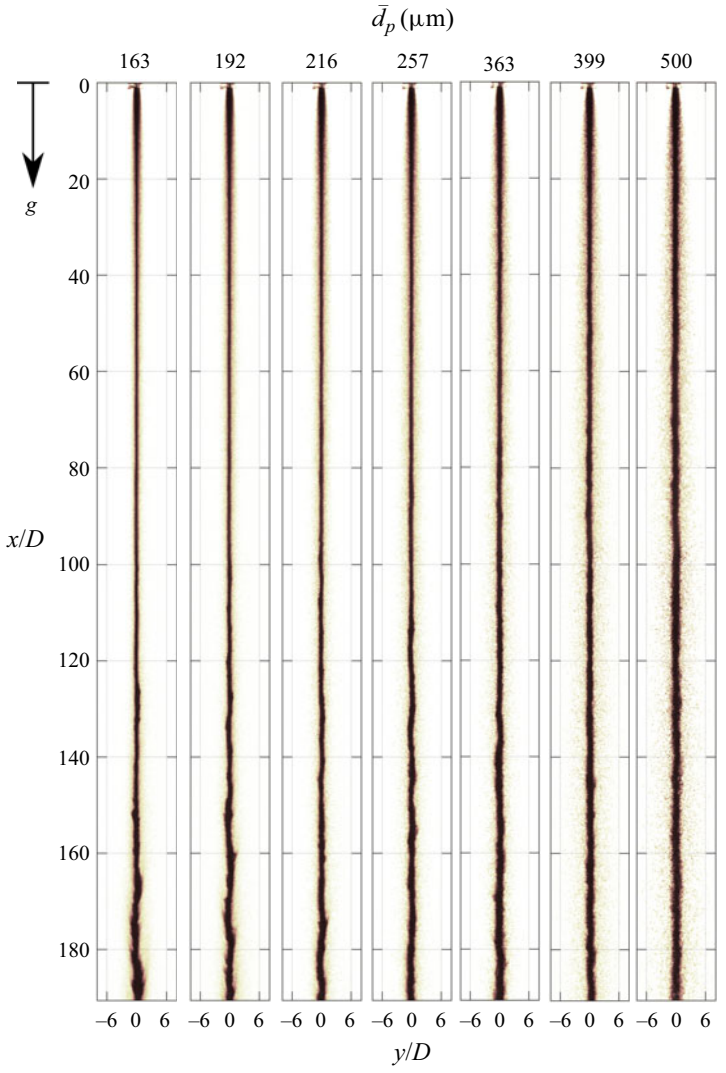

Figure 7. Instantaneous side-view images of the particle curtain $0 \lesssim x \lesssim 940$ mm for seven different particle sizes ($\bar{d}_p$). Here, the hopper outlet thickness (D) is constant at 5 mm. The particle flow is from top to bottom following the gravitational direction (g).

outlet thickness. This suggests that the mechanism that causes the particles to disperse laterally away from the hopper centreline in the near field is relatively insensitive to particle size. Furthermore, the larger particles disperse further away (laterally) from the curtain centreline in the near field than do the smaller particles for all hopper outlet thicknesses. This is attributed to the greater inertia of the larger particles. That is, larger particles will be transported further away from the centreline than smaller particles, due to their greater lateral momentum relative to the drag force.

Further downstream from the initial expansion region, for all cases except for the largest particles ($\bar{d}_p = 500\,\mu$m) issuing from the smallest hopper ($D = 3$ mm), the curtain thickness exhibits a local maximum (a peak). The location of this local maximum, x_{pk} is approximately within the region $5 \lesssim x_{pk}/D \lesssim 26$ for all cases, with this location

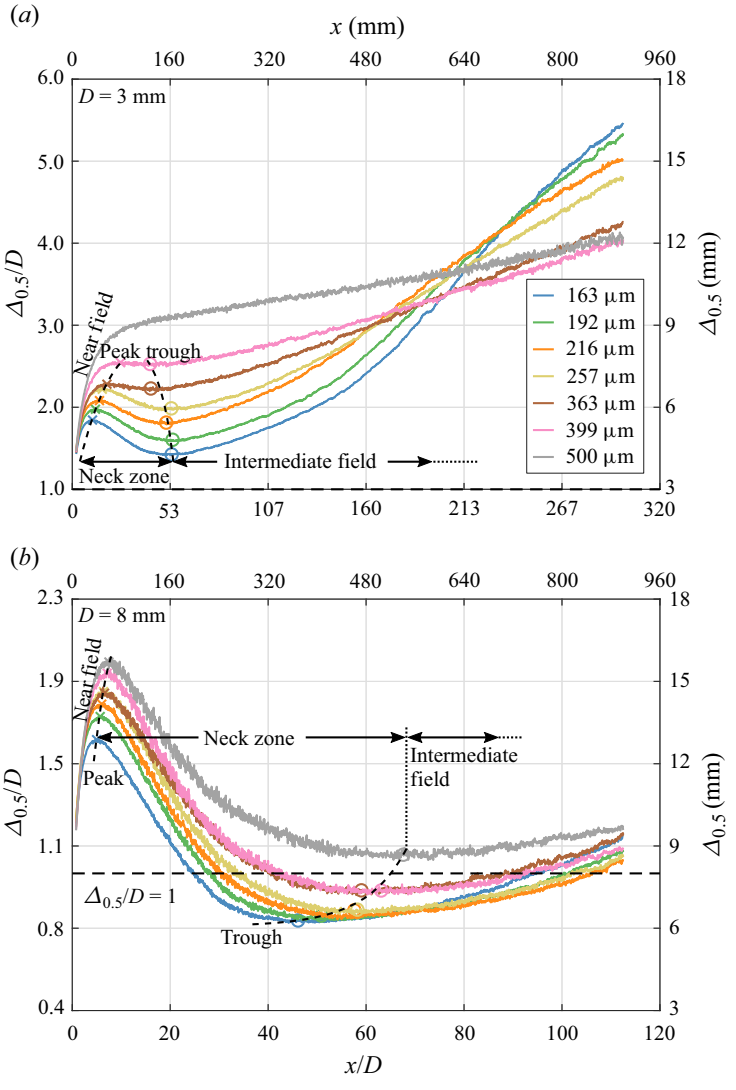

Figure 8. Axial variation of the free-falling particle curtain thickness ($\Delta_{0.5}$), defined as the full width at half-maximum, measured for seven different particle diameters for cases of (*a*) $D = 3$ mm and (*b*) $D = 8$ mm. Note that there are two labels for the *y*-axes, one for the non-normalised curtain thickness ($\Delta_{0.5}$), and the other for the curtain thickness normalised by hopper outlet thickness ($\Delta_{0.5}/D$). The circles and x symbols denote the locations of the local minima and maxima of $\Delta_{0.5}$ for each case.

shifting further downstream as the particle size is increased. This is consistent with the larger particles having greater momentum (relative to drag) than the smaller particles. The prominence of the local maximum appears to decrease with an increase in particle diameter and a decrease in hopper outlet thickness, i.e. for greater values of $\bar{d}_p/D$. For the case where $\bar{d}_p/D$ is the greatest, i.e. $\bar{d}_p/D = 1/6$, which occurs with the largest particles ($\bar{d}_p = 500\,\mu$m) and the smallest hopper ($D = 3$ mm), the peak disappears completely, as previously noted. That is, this case does not exhibit a neck zone.

Where a local maximum occurs, it is followed by a region in which the curtain thickness decreases with downstream distance, before increasing again. This is the well-known

'necking' effect (Hardalupas, Taylor & Whitelaw 1989; Lau & Nathan 2014, 2016; Ho *et al.* 2017), where the streamwise acceleration of particles becomes significant, leading to a decreased local pressure within the curtain. This, in turn, results in particles (and fluid) being drawn towards the centreline. The curtain thickness typically continues to decrease for a few hundred millimetres downstream until $40D \lesssim x \lesssim 80D$ where $\Delta_{0.5}/D$ reaches a local minimum (a trough), before it begins to expand again. The latter marks the beginning of the intermediate-field expansion region. That is, downstream of the local minimum, the curtain thickness expands, presumably due to the entrainment of surrounding gas into the curtain, consistent with the well-known dynamics of particle-laden jets (Longmire & Eaton 1992; Lau & Nathan 2016). It should be noted that, in the intermediate field, the gravity-driven acceleration of the particles is expected to be relatively small, with the drag forces dominating over the gravity-driven forces such that the curtain approximates a jet. Near to the end of the measurement region, the expansion of the curtain approaches a linear function, with the rate of expansion (i.e. the gradient of the curves in figure 8) increasing as the particle diameter is decreased. This is because smaller particles, with their lower inertia, are expected to have a stronger interaction with the ambient air, causing smaller particles to spread more rapidly than the larger particles (Lau & Nathan 2016).

The results also show that the maximum curtain thickness in the near-field expansion region, $\Delta_{0.5,pk}/D$, typically decreases with an increase in the hopper outlet thickness. For example, in the cases of $\bar{d}_p = 163\,\mu$m particles, $\Delta_{0.5,pk}/D \approx 1.85$ for the hopper of $D = 3$ mm, decreasing to $\Delta_{0.5,pk}/D \approx 1.61$ for the hopper of $D = 8$ mm. This suggests that a normalisation of the curtain thickness by the hopper outlet thickness does not result in the self-similarity profiles in flow thickness that are observed in jets (Mi, Nobes & Nathan 2001). This difference is not surprising, but implies that the mechanisms controlling the initial curtain expansion does not scale with D alone.

Figure 9 presents an example of the curtain side view illustrating the boundaries of the dilute-particle region and the curtain core defined by 5 % and 50 % of the peak opacity, i.e. $\Delta_{0.05}$ and $\Delta_{0.5}$. The dilute-particle region is clearly differentiated from the curtain core by a much lower volume fraction. The radial profiles do not vary very much with axial distance, which implies that the radial movement of the particles is weak. The 5 % contour is well above the noise threshold at $|y/D| > 4$, giving confidence in the choice of boundary. These boundaries are also reliable for $|y/D| < 1$.

Figure 10 presents the time-averaged measurements of the axial evolution of total thickness of the dilute-particle region, accounting for both sides of the curtain core region for seven particle sizes ($\bar{d}_p = 163$, 192, 216, 257, 363, 399 and 500 μm) and for two hopper outlet thicknesses ($D = 3$ and 8 mm). This dilute-particle region is defined by a difference of curtain thicknesses between 5 % and 50 % of the peak opacity at the lateral plane, that is $\Delta_{0.05} - \Delta_{0.5}$. The results show that $\Delta_{0.05} - \Delta_{0.5}$, for $x/D < 10$, increases from a non-zero value near to the hopper outlet to a value some two times the hopper outlet thickness, which is of the same magnitude as that for $\Delta_{0.5}$, as shown in figure 8. Furthermore, the largest particles expand the most. This indicates that the dilute-particle region originates from the near-exit region, where inter-particle collisions and particle–hopper interactions generate significant particle lateral momentum, causing the initial dispersion, as previously discussed. That the outer layer of the particles is not entrained back into the curtain core implies that the initial expansion moves them into a region of negligible radial pressure gradient, including that induced by particle acceleration in the neck zone of the curtain core (figure 8). That is, these particles are not re-entrained into the curtain.

For $x/D > 130$ ($D = 3$ mm) and 60 ($D = 8$ mm), there is a second noticeable increase of the regional thickness for the smallest particles. This coincides with the region of

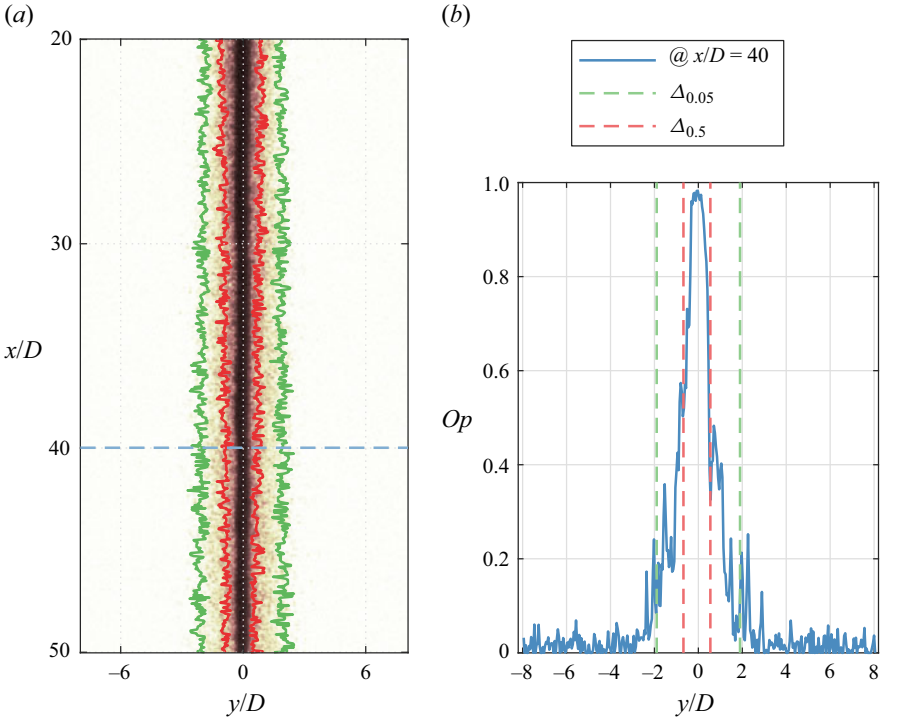

Figure 9. The contours of the half-width, $\Delta_{0.5}$ (red line) and the contours of 5 % of the peak opacity $\Delta_{0.05}$ (green line), defining the boundaries of the dilute-particle region, as presented in (*a*), the axial evolution and (*b*) the radial profile at $x/D = 40$. Here, $D = 5$ mm and $\bar{d}_p = 270\,\mu$m.

intermediate-field expansion as identified in figure 8, with a higher expansion rate for the smaller $\bar{d}_p$. The consistency in particle expansion between these two lateral regions implies a common controlling mechanism – namely that both are in the drag-dominated regime where smaller particles have a higher drag per unit volume ratio, therefore expanding faster. In contrast, the larger particles, $\bar{d}_p = 257 \sim 500\,\mu$m, do not show the same expansion. This suggests the persistence of the upstream mechanisms throughout the downstream region.

Figure 11 presents a schematic diagram of the side view of the falling particle curtain, together with the notation used to characterise the near- and intermediate-field expansions in the flow. The magnitudes of the local 'peak' and 'trough' features of the curtain thickness are denoted by $\Delta_{0.5,pk}$ and $\Delta_{0.5,tr}$, respectively, with their corresponding streamwise locations measured from the hopper exit represented by x_{pk} and x_{tr}, respectively. The gradients of expansion in the near field and the intermediate field are denoted separately by K_{near} and K_{int}, with both defined as the differentiation of the full curtain thickness over a specific streamwise location defined as appropriate below.

This image also reveals more details about the source of the particles that are found at low number density in the outer 'dilute-particle' region that surrounds the dense particle curtain, denoted by $\Delta_{0.05} - \Delta_{0.5}$. The generation of this region of more dispersed particles is important because they are likely contributors to the generation of fine particle emissions that can readily migrate from a curtain by being entrained into secondary flows within a falling particle receiver or other types of equipment. This image suggests that these

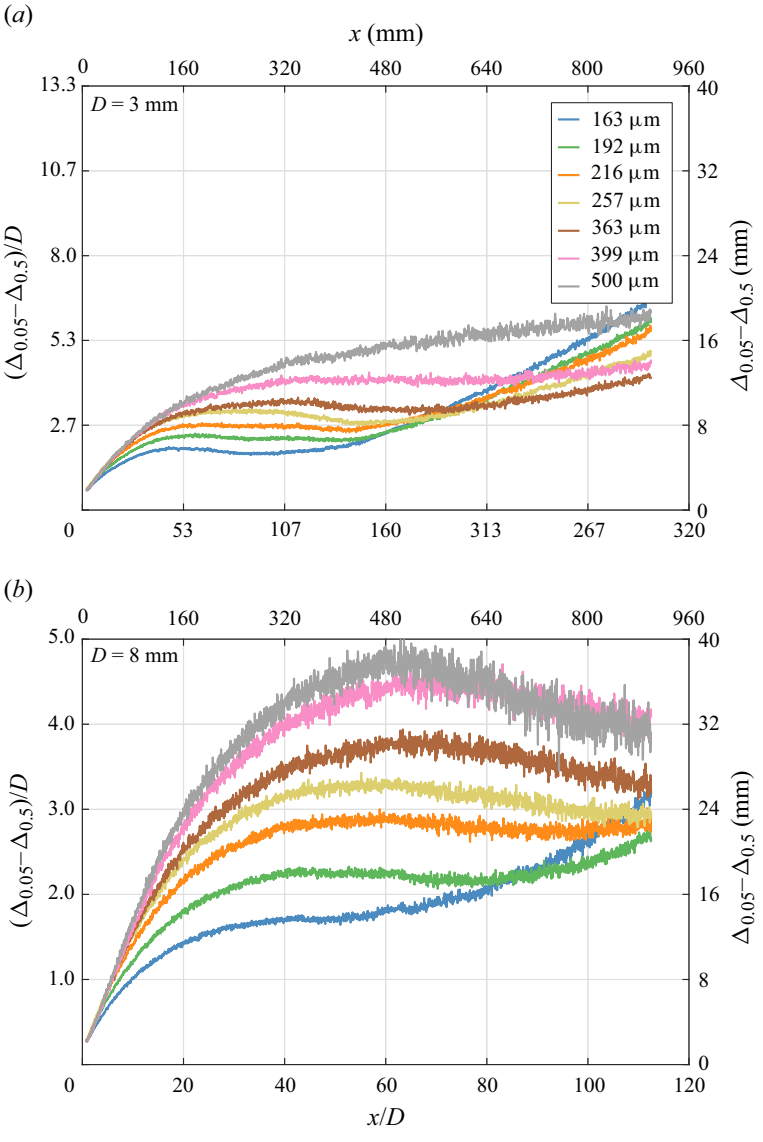

Figure 10. Axial evolution of the dilute-particle region characterised by the difference of curtain thicknesses $\Delta_{0.05} - \Delta_{0.5}$, normalised by hopper outlet thickness D, for cases of (*a*) $D = 3$ mm and (*b*) $D = 8$ mm with seven different particle sizes ($\bar{d}_p$).

particles originate from the near-field expansion region, where the collision-induced force disperses them beyond the range at which they can be re-entrained into the jet.

Figure 12 presents the gradient of the near-field expansion (K_{near}) and the intermediate-field expansion (K_{int}) as a function of normalised particle diameter, $\bar{d}_p/D$, for all examined particle diameters and hopper outlet thicknesses. These values were obtained by curve fitting a linear function to the data in the near-field expansion region ($0 \lesssim x/D \lesssim 13$), and the downstream region of the intermediate field ($76 \lesssim x/D \lesssim 300$) where the evolution of $\Delta_{0.5}/D$ with axial distance is approximately linear. For all cases, the linear curve fits have a coefficient of determination, $R^2 \approx 95\,\%$. The results from figure 12(*a*)

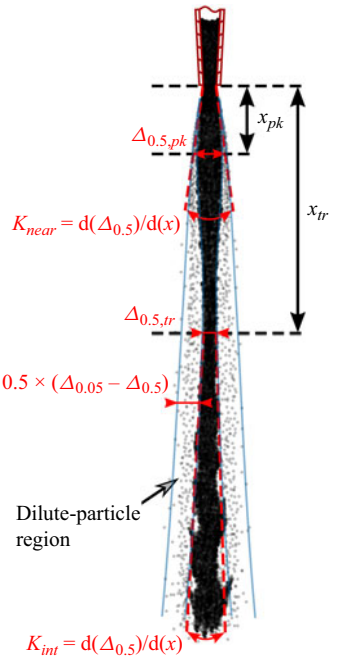

Figure 11. Schematic diagram of the curtain side view, together with the notation used to describe the key features of the local peak (subscript 'pk') and trough (subscript 'tr') that characterise the curtain thickness $\Delta_{0.5}$. The gradients of the expansion in the near field and the intermediate field are denoted by K_{near} and K_{int}. The 'dilute-particle' region with particles dispersed around the denser curtain 'core' region, as denoted by $\Delta_{0.05} - \Delta_{0.5}$, is also shown.

show that K_{near} is typically an order of magnitude larger than K_{int} from figure 12(*b*) for all cases. The near-field expansion gradients found here, $0.0796 \leq K_{near} \leq 0.1703$, translate to a near-field expansion half-angle in the range $2.3^\circ \leq \alpha \leq 4.8^\circ$. The near-field expansion rate was also found to increase with hopper outlet thickness for almost all normalised particle diameters ($\bar{d}_p/D$), while only being weakly dependent on the particle diameter, consistent with the measurements (figure 8). Although particle initial momentum is based on particle inertia, which depends on particle diameter, this finding suggests that particle lateral momentum is gained mostly from the increase in D. This increases the fraction of particles within the flow that are unaffected by drag at the wall, thereby increasing the particle axial momentum and, in turn, the lateral momentum that arises from inter-particle collisions in the near field. Such collisions occur because the particles near to the hopper internal wall fall more slowly than those closer to the centreplane. In addition, a higher particle volume fraction at the exit was found to be associated with a larger D (Janda *et al.* 2012; Wang *et al.* 2020), which also increases the near-field expansion of the particle curtains by enhancing particle–particle collisions.

Interestingly, the rate of expansion in the intermediate field shows the opposite trend to that in the near field, with the intermediate-field expansion rate increasing as both the hopper outlet thickness and the particle diameter are decreased, as shown in figure 12(*b*). This implies a different controlling mechanism of the particle curtain dynamics in this region compared with that in the near field. The general trend of decreased values of K_{int} with an increase in D is consistent with the Beverloo equation, which shows that the mass flow rate, and hence momentum, scales with $D^{1.5}$. That is, the influence of

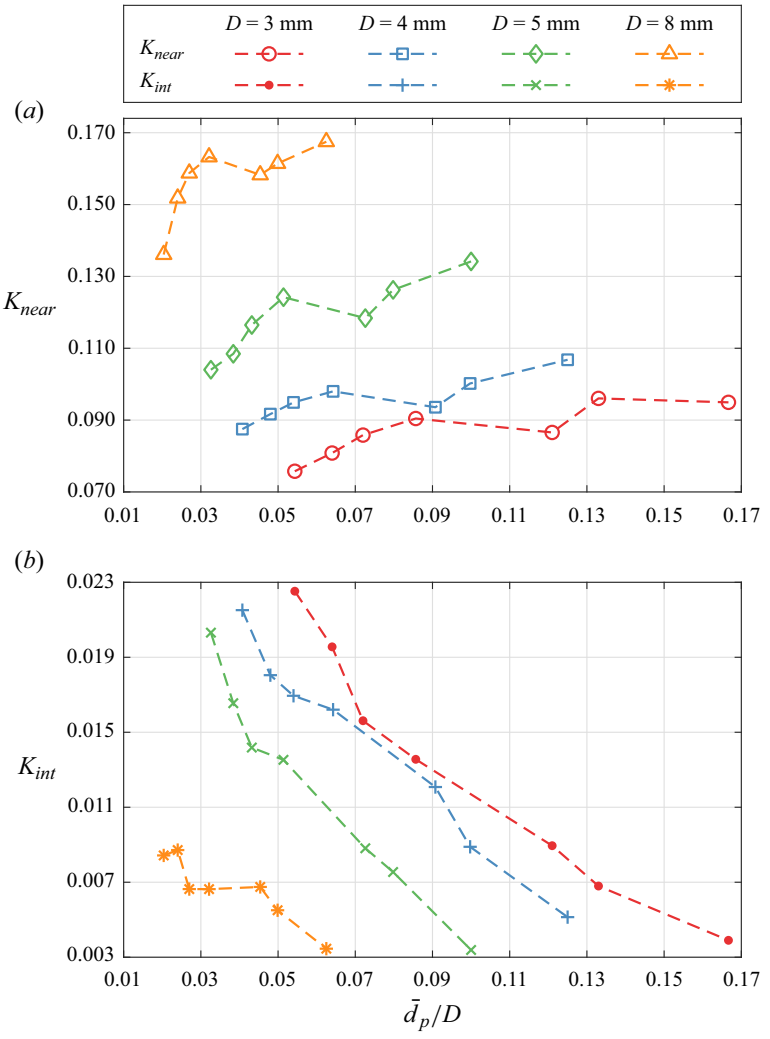

Figure 12. The dependence of the linear gradients of (*a*) the near-field expansion, K_{near} and (*b*) the intermediate-field expansion, K_{int} on the normalised particle diameter ($\bar{d}_p/D$) for a series of hopper outlet thicknesses ($D = 3$, 4, 5 and 8 mm). Gradients are obtained through curve fitting of the curtain thickness axial profiles (see figures 8 and 11).

particle inertia is greater for larger hopper outlet thickness. This influence may also be compounding, since a lower spreading rate will also lead to higher local volume fractions. Previous work has shown that, where the volume fraction is sufficiently high, the presence of downstream particles can reduce the drag of the upstream particles due to the effect of aerodynamic wake (Cooper & Arnold 1995; Wang *et al.* 2016; Sedaghatizadeh *et al.* 2022). Here, we call it the 'particle group wake' (or the particle 'group effect') to highlight its bulk effect on the particle stream. This, in turn, will further reduce the expansion rate due to the reduced entrainment into the curtain. This trend has also been found to occur further downstream for a particle stream issuing from a round hopper, although the flow regimes are significantly different from those identified in the present study (Wang *et al.* 2016). In addition, the results also show that K_{int} increases with a decrease in $\bar{d}_p$, with K_{int} exhibiting a stronger dependence on particle size than K_{near}. This highlights the

importance of particle–air interaction through the shear force between the particles and the surrounding fluid, which dominates the intermediate-field expansion in a jet-like flow regime, consistent with the results presented in figure 8.

Figure 13 presents the relative axial streamwise positions of the local peaks and troughs in the curtain thickness profiles, x_{pk}/D or x_{tr}/D, and their relative magnitudes, $\Delta_{0.5,pk}/D$ or $\Delta_{0.5,tr}/D$, as identified from figure 8 and illustrated in figure 11, as a function of normalised particle size ($\bar{d}_p/D$). In particular, figure 13(*a*) shows that the value of x_{pk}/D for any given hopper outlet thickness increases monotonically with the particle size. This is consistent with the momentum of particles relative to the drag force being greater for larger particles, as previously discussed. The influence of particle diameter on x_{pk}/D can be illustrated using a simplified model comprising a single spherical particle in a quiescent environment imparted with an initial radial (or lateral) velocity in the Stokes regime. Under these conditions, the equation of motion for the particle is

$$\frac{\partial V_p}{\partial t} + \frac{V_p}{\tau_p} = 0, \tag{4.3}$$

where V_p is the particle velocity in the radial direction (i.e. the y-direction). Solving this equation for particle radial displacement results in $y_p(t) = \tau_p V_0[1 - \exp((-t)/\tau_p)]$, where y_p is the displacement of the particle from the centreplane and V_0 is the particle initial velocity in the radial direction. Therefore, the radial distance required for the particle to reach a radial velocity component of zero is $\propto \tau_p$. Since $\tau_p \propto \bar{d}_p^2$, this implies that y_p and hence x_{pk}/D are also positively correlated with $\bar{d}_p^2$ ignoring any differences in K_{near} for different particle sizes shown in figures 8 and 12.

Figure 13(*a*) also shows that the profiles of x_{tr}/D for the four different hopper outlet thicknesses collapse quite well to a single arch-shaped curve, with the maximum x_{tr}/D appearing for $\bar{d}_p/D \approx 0.05$, although the flow inside the hopper was previously found to be independent of particle size for $\bar{d}_p/D < 0.05$ (Beverloo *et al.* 1961). As the neck zone is formed by particle–air interaction, the local 'trough' of the particle curtain thickness established at the end of this region depends on the balance between particle inertia, which drives the near-field expansion, and the influence of the entrained surrounding air induced by particle acceleration that drives particles toward the curtain 'core'. That is, the larger particles in the range $\bar{d}_p/D > 0.05$ have a higher ratio of inertia to drag, so that they tend to retain their original trajectory to disperse away from the curtain core, while the relatively smaller hopper outlet thickness within $\bar{d}_p/D > 0.05$ cannot generate sufficient pressure difference in the fluid phase between curtain core and surroundings to entrain these larger particles back to the curtain core. This results in lower values of x_{tr}/D and of $\Delta_{0.5,tr}/\Delta_{0.5,pk}$, indicating that particles in the range $\bar{d}_p/D > 0.05$ become less responsive (less necking) to the pressure gradient as particle size increases. Indeed, no neck zone at all is formed for the extreme case of $D = 3$ mm and $\bar{d}_p = 500\,\mu$m, as can be seen in figure 8(*a*). In contrast, the smallest particles exhibit the opposite trend due to their stronger dependence on aerodynamic drag, leading to the most significant necking effects. That is, x_{tr}/D decreases with an increase in $\bar{d}_p/D$ for $\bar{d}_p/D > 0.05$.

While particle accelerations were not directly measured in the present study, they can be estimated using the Stokes assumption (3.5). The calculated accelerations for $D = 3$ mm, with seven different values of $\bar{d}_p$ are shown in figure 14. As can be clearly seen, the particle acceleration decreases with an increase in x and a decrease in $\bar{d}_p$. The negative correlation of x_{tr}/D with particle size for $\bar{d}_p/D > 0.05$ can therefore be attributed to the increase in particle acceleration with particle diameter, owing to their stronger dependence on gravity than on drag, resulting in a greater acceleration closer to the exit plane.

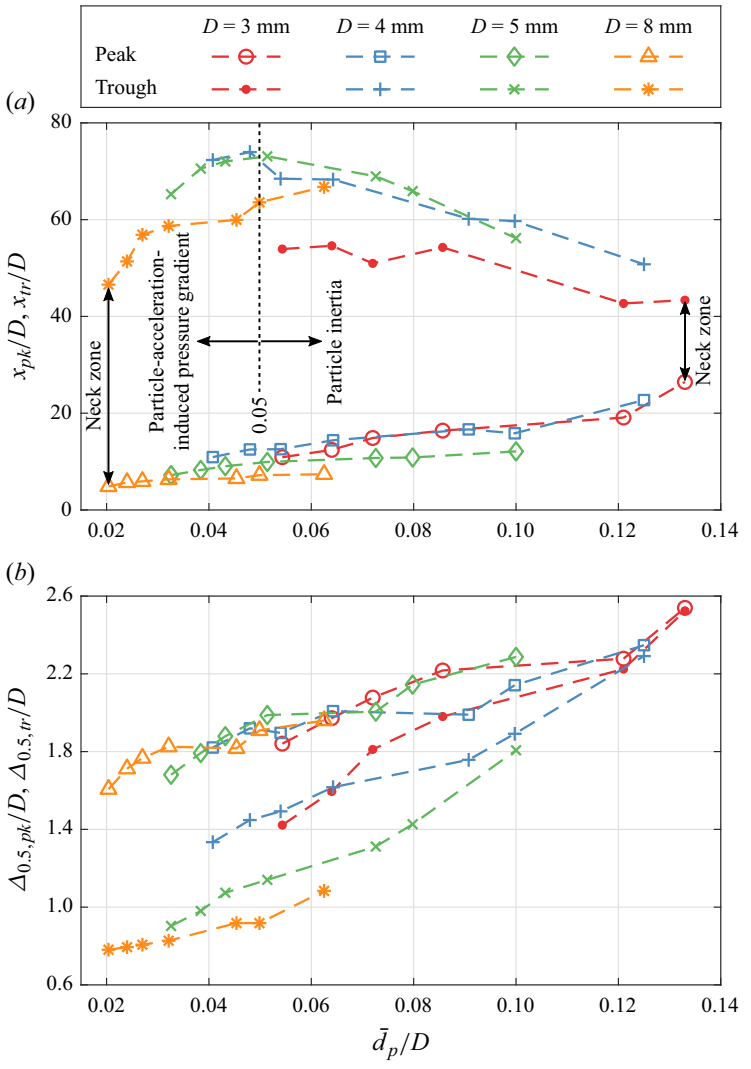

Figure 13. The influence of normalised particle diameter ($\bar{d}_p/D$) on the streamwise locations of the local peaks, x_{pk}/D, and troughs, x_{tr}/D, in the curtain thickness axial profiles (see also figures 8 and 11), together with the magnitudes of the peaks, $\Delta_{0.5,pk}/D$ and troughs, $\Delta_{0.5,tr}/D$, for a series of hopper outlet thicknesses ($D = 3$, 4 ,5 and 8 mm).

For $\bar{d}_p/D < 0.05$, the particle acceleration plausibly generates a lateral pressure gradient of sufficient magnitude for the drag of the entrained fluid to become significant relative to particle inertia. As a result, the larger particles of $\bar{d}_p/D < 0.05$ are no longer able to follow their original spreading trajectory but rather move towards to the curtain core. This can be directly observed from figure 8(*b*), where a neck zone is even generated for $\bar{d}_p = 500\,\mu$m. However, the process of contraction requires a longer distance and is also less prominent for the larger particles, due to their lower ratio of drag to inertia. Therefore, the neck zone in the range of $\bar{d}_p/D < 0.05$ can be deduced to be dominated by hopper-controlled particle acceleration, which induces significant pressure gradient.

Figure 13(*b*) presents the relative magnitudes of the thickness of the peaks (local maxima) and troughs (local minima), $\Delta_{0.5,pk}/D$ or $\Delta_{0.5,tr}/D$, as a function of $\bar{d}_p/D$ for

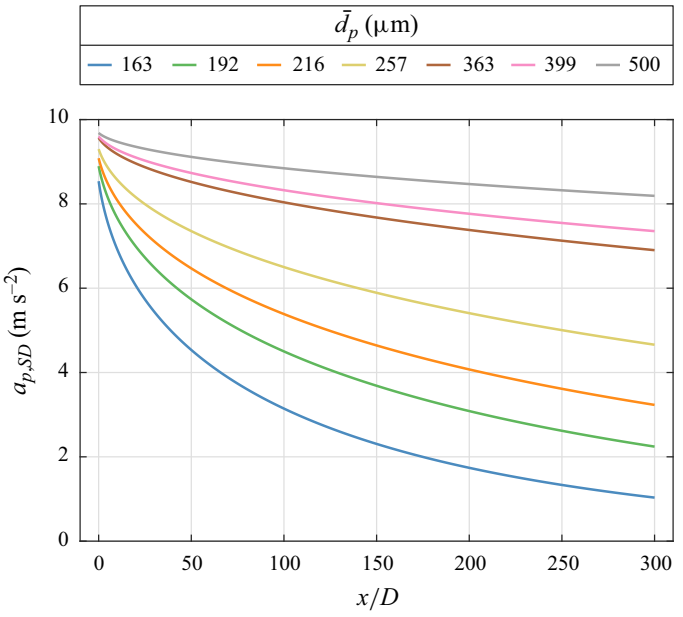

Figure 14. The axial evolution of the particle axial acceleration calculated with the simplified analytical model in the Stokes regime (3.5) for seven different particle sizes and for $D = 3$ mm.

$D = 3, 4, 5$ and 8 mm. The results show that, for all cases, $\Delta_{0.5,pk}/D$ is significantly greater than the hopper outlet thickness, with $1.61 \leq \Delta_{0.5,pk}/D \leq 2.54$ across all examined conditions. That is, the actual thickness of the particle curtain can be up to a factor of 2.5 greater than the hopper outlet thickness, even in the near field. Furthermore, the results show that the difference between $\Delta_{0.5,pk}$ and $\Delta_{0.5,tr}$ decreases with an increase in $\bar{d}_p/D$. That is, the near-field expansion and necking are more prominent with larger hopper outlet thickness and smaller particle sizes, consistent with figure 8. For this reason, an increase in $\bar{d}_p/D$ also causes the values of $\Delta_{0.5,pk}$ to approach $\Delta_{0.5,tr}$ and, for sufficiently large $\bar{d}_p/D$, the values of $\Delta_{0.5,pk}$ and $\Delta_{0.5,tr}$ may eventually converge, at which point the neck zone ceases to exist, as can also be seen in figure 8(*a*). Indeed, the measurements of $\Delta_{0.5,pk}$ and $\Delta_{0.5,tr}$, together with x_{pk}/D and x_{tr}/D, for the smallest hopper outlet thickness of $D = 3$ mm and the largest particle size of $\bar{d}_p = 500\,\mu$m are not presented in figure 13 because no peak or trough exists for this case.

The results also show that $\Delta_{0.5,pk}/D$ increases approximately linearly with $\bar{d}_p/D$ and the profiles for all four different hoppers collapse well with these axes. The increase in $\Delta_{0.5,pk}/D$ with particle diameter is attributed to the greater momentum (relative to drag) of the larger particles, as previously discussed. Together with the finding from figure 13(*a*), it can be deduced that both the location and the magnitude of the peaks at the near-field expansion scale with the particle size and hopper outlet thickness, potentially highlighting the influence of the particle–particle and particle–wall interactions as being the dominant mechanisms controlling the flow dynamics in the near-field expansion region. This finding of the dominant mechanisms is consistent with the trends identified previously for the influence of hopper on the near-field flow region using a round hopper outlet (Wang *et al.* 2016).

Figure 14 presents the evolution of particle axial acceleration ($a_{p,SD}$) calculated with the simplified analytical model in the Stokes regime (3.5). The smaller particles present

a lower $a_{p,SD}$ throughout the examined falling distance, although the starting $a_{p,SD}$ is similar for the various $\bar{d}_p$. The smaller particles also undergo a faster decay of particle acceleration in the axial direction, decreasing to more than half of the starting $a_{p,SD}$ at the first $100D$, due to their higher drag per unit volume ratio. In contrast, the largest particle $\bar{d}_p = 500\,\mu\text{m}$ continues preserving the high acceleration due to a greater influence of gravitational acceleration.

4.3. *Particle curtain transmittance*

Figure 15 presents seven representative instantaneous images of measured curtain transmittance, each with a different particle diameter, here all obtained with hopper $D = 5\,\text{mm}$. A qualitative trend can be seen in which the curtain transmittance is low near to the exit and increases with downstream distance. This overall trend is consistent with previous investigations (Ogata *et al.* 2001; Sedaghatizadeh *et al.* 2022), and is due to the particle velocity increasing with downstream distance (due to the acceleration of gravity), resulting in a decrease in local particle number density with streamwise distance and an increase in transmittance. However, the higher resolution of the present images provides additional detail over what has been reported previously. In particular, it can be seen that the distance to the streamwise location at which the opacity begins to fall decreases with an increase in particle diameter. Furthermore, the region downstream from this location exhibits significant instantaneous structure, which can be deduced to be driven by large-scale flow instabilities.

The overall trend of a decrease in the distance at which transmittance begins to increase with particle diameter is consistent with the increase in particle acceleration (see figure 14). That is, the axial spacing between particles depends on acceleration, which increases with $\bar{d}_p$. This is also consistent with the previous measurements using hoppers with rectangular outlets, which show that particle velocity increases with $\bar{d}_p$ and with axial distance (Kim *et al.* 2009; Sedaghatizadeh *et al.* 2022). In addition, the particle cross-sectional area per unit volume also decreases with an increase in $\bar{d}_p$, which will lead to a greater T for a given hopper outlet thickness.

The position of the local maximum in curtain thickness at the end of the near-field expansion region, x_{pk}/D, and the location of the local minimum curtain thickness at the end of the neck zone, x_{tr}/D (see also figure 11), are also shown in figure 15 (with the red and blue lines, respectively). It can be seen that both of these features occur well upstream from the point at which the opacity begins to fall noticeably, with no clear correlation between the locations of x_{pk}/D and x_{tr}/D and local values of light transmittance. The lack of a direct influence is because these features cause a difference in lateral spacing (along the y-axis) between particles, rather than axial spacing, while the transmittance of the particle curtain is mostly dependent on the axial spacing between particles.

The instantaneous images presented in figure 15 also reveal the presence of highly localised regions of low curtain transmittance, with these regions typically consisting of filament-like or rope-like structures that have long axial coherence. These structures are typically aligned in the streamwise direction, with their span being of the same order as the local thickness of the curtain. This is consistent with the presence of particle 'clusters', which have been demonstrated to exist in a range of particle-laden jets (Lau & Nathan 2017; Lau, Frank & Nathan 2019). Here, the term 'cluster' is used following the pioneering work of Longmire & Eaton (1992) and Eaton & Fessler (1994) to refer to local groups of particles whose spacing is significantly less than average due to the role of large-scale flow features, but does not imply that any particles actually touch each other to

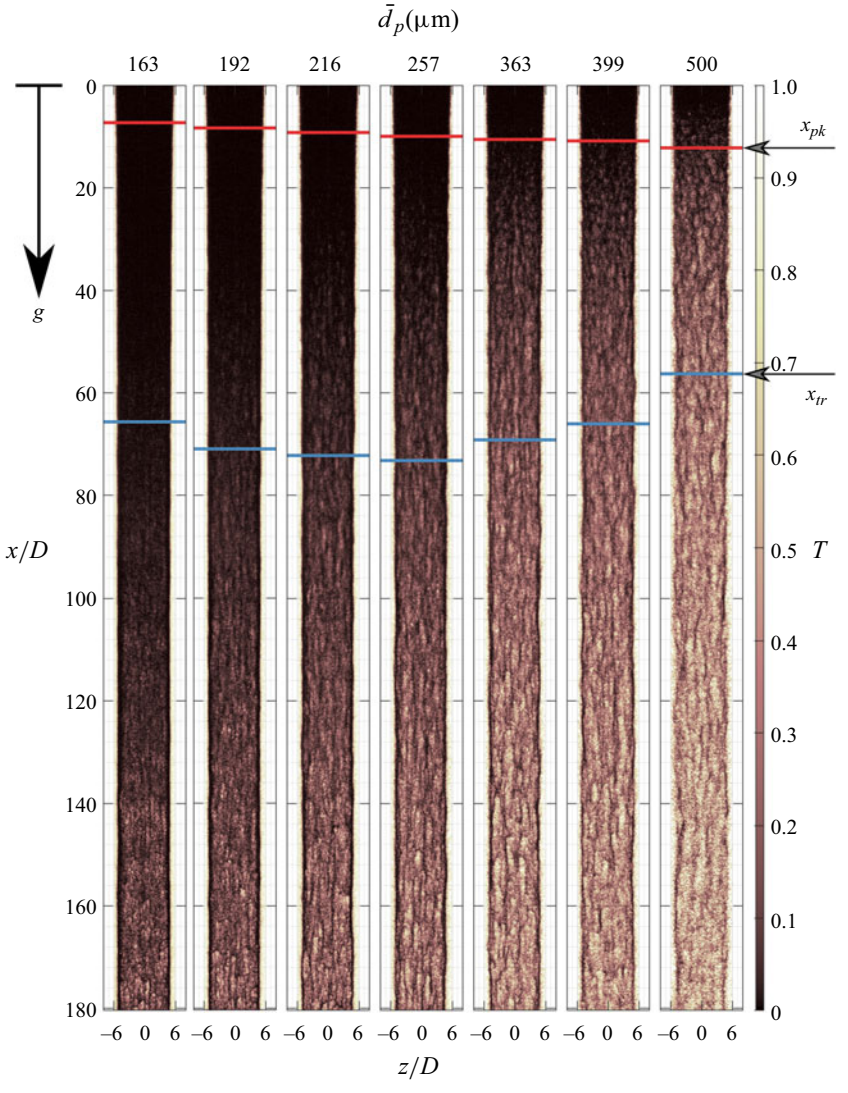

Figure 15. Instantaneous front-view images of the particle curtain issuing from a rectangular hopper of $D =$ 5 mm, recorded at a falling distance between 0 and ≈900 mm from the hopper exit, for seven different particle diameters ($\bar{d}_p$). The positions of x_{pk} and x_{tr} (see also figure 11) are shown with red and blue lines, respectively. Here, the particle flow is from top to bottom following the direction of gravity.

form aggregates. These clusters are typically characterised by highly localised regions of high particle number density within the flow, and are typically caused by the interaction of the particles with the fluid flow (Maxey 1987; Squires & Eaton 1991; Longmire & Eaton 1992; Eaton & Fessler 1994; Capecelatro, Desjardins & Fox 2015). Whatever their origin, the effect of these clusters is to induce local, instantaneous non-uniformity in transmittance, that is to both reduce transmittance locally where the clusters are present, and to increase the transmittance on either side of the clusters. The presence of these clusters is particularly significant for applications such as FPRs, as the increased transmittance in non-clustered regions may result in solar radiation passing through the curtain, potentially damaging internal walls and surfaces. Additionally, the particles within

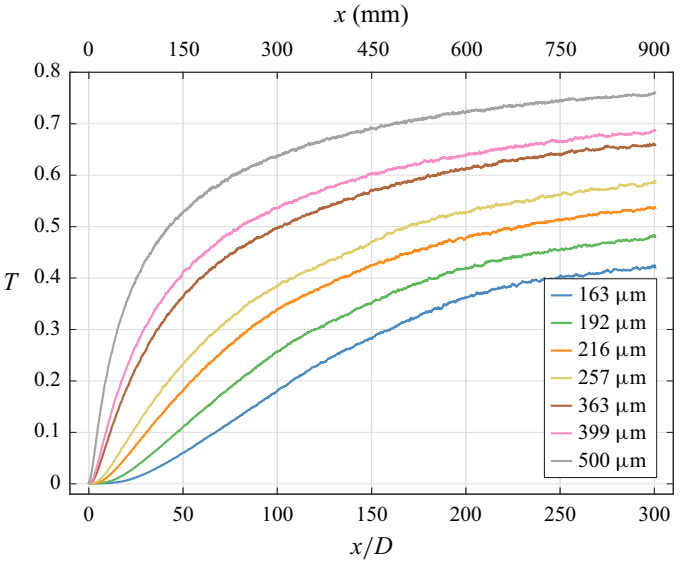

Figure 16. Experimental measurements of time-averaged particle curtain transmittance as a function of particle falling distance, x, normalised by the hopper outlet thickness (D) for seven different particle diameters. In this case, the hopper outlet thickness was fixed at $D = 3$ mm.

the clusters may be shadowed from solar radiation due to their high opacity, resulting in lower average particle temperatures. These images also highlight the need to better understand the origins of these clusters, the need to be able to identify the axial distance at which they become significant and the need for methods to manage or account for their influence. Furthermore, the clear presence of these particles in almost all cases also implies that current steady-state models, both analytical and numerical, are likely to be unreliable in regions where clustering is significant.

Figure 16 presents the time-averaged curtain transmittance as a function of the falling distance for seven different particle sizes and for a fixed hopper outlet thickness $D = 3$ mm. The results show that the slope of the initial rise of transmittance depends strongly on the particle diameter. For the largest particle, this slope is high, so that T increases strongly within the first $20D$. In contrast, the initial slope is near to zero for the smallest particles. These trends are consistent with the visual observations shown in figure 15 and the accompanying discussion, with more details to support these deductions being derived from the analysis below. The slopes of the transmittance axial profiles reduce beyond a falling distance of approximately $50D$, with monotonically consistent trends (almost parallel curves) in the relationship between T and x/D for all cases of different $\bar{d}_p$ at the end of the measurement window. This former trend can be explained by a much stronger decrease in particle acceleration with axial distance for smaller particles than larger particles, when approaching the terminal velocity (see figure 14). That is, the rate of acceleration decays much faster for smaller particles than larger ones, which reduces the rate of increase in particle vertical separation and the rate of increase in transmittance. However, the latter trend regarding the near-parallel and asymptotically stable profiles of T between different $\bar{d}_p$ can be attributed to the relatively lower decay rate of particle acceleration. This trend also suggests a simpler regime for the curtain transmittance than for the curtain expansion under the effect of $\bar{d}_p$, which can be further discovered by a normalisation of the data.

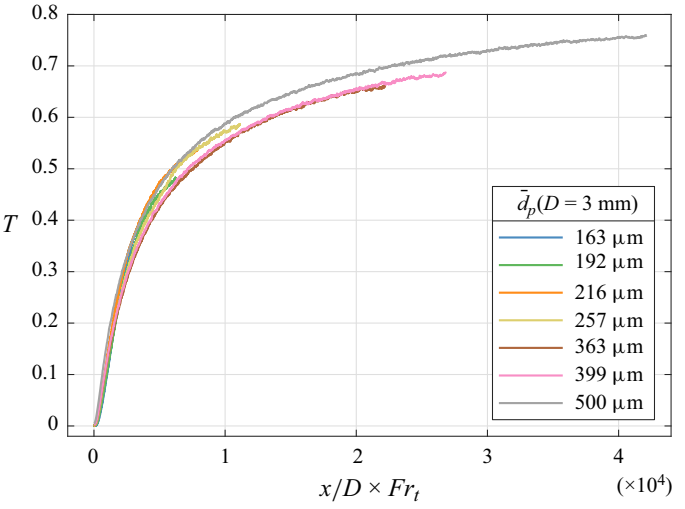

Figure 17. Measured particle curtain transmittance as a function of particle falling distance (x) normalised by the hopper outlet thickness (D) and the terminal Froude number (Fr_t) for seven particle sizes. The value of Fr_t was calculated using the particle terminal velocity estimated from the analytical model in the Stokes regime, $U_{t,SD}$ (3.4).

Figure 17 presents the same particle curtain transmittance as plotted in figure 16, except that the data are now plotted as a function of the particle falling distance that is normalised by the hopper outlet thickness and particle Froude number based on the estimated particle terminal velocity (using the Stokes-drag model, as discussed in § 3.2), $Fr_t = U_{t,SD}/(gD)^{0.5}$. The data are only plotted for $D = 3$ mm because of the most dispersed particle condition, which best suits the adopted model. It can be seen that this normalisation provides a good collapse of the cases with different values of $\bar{d}_p$ onto a single curve. This highlights the dependence of the transmittance on the gravity-driven evolution of particle vertical velocity. It is also consistent with previous findings that the magnitude of particle streamwise velocity depends on Fr_t (Sedaghatizadeh *et al.* 2022). The collapse with the current normalisation also provides evidence that the balance between the inertial and gravitational forces dominates the evolution of particle vertical velocity rather than any influences of the shear forces in the shear layer, at least in this set comparing different values of $\bar{d}_p$.

Figure 18 presents the measured values of time-averaged curtain transmittance (T) as a function of the falling distance for four different hopper outlet thicknesses ($D = 3$, 4, 5 and 8 mm), but with a fixed particle size $\bar{d}_p = 363$ μm. This shows that, somewhat analogously to figure 16, the initial rate at which T increases also varies greatly, from a high slope for $D = 3$ mm, to a near-zero initial slope for $D = 8$ mm. Taken together with figures 15 and 16, this shows that the axial distance to the point at which the transmittance starts to increase rapidly with axial distance increases with both an increase in D and a decrease in $\bar{d}_p$. This is partially attributed to the higher particle volume fraction for using a greater D, as discussed before. That is, using a hopper with a larger D increases the particle volume fraction significantly at the near-exit region which, in turn, causes a dramatic difference in the axial profile of curtain transmittance. However, this difference reduces with the axial distance as particles fall downwards, influenced by varying particle–fluid interactions depending on the size of D. The bulk-average particle–fluid interaction with curtain expansion is expected to be stronger for a smaller D due to the reduced influence of

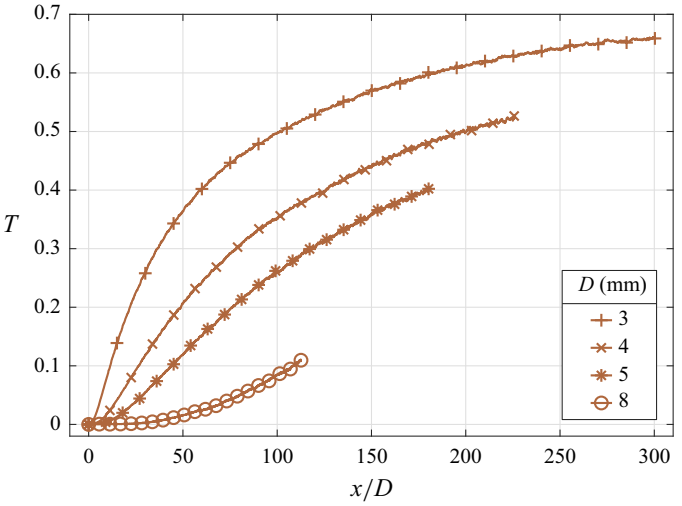

Figure 18. Experimental measurements of time-averaged particle curtain transmittance as a function of normalised particle falling distance, x/D, for four different hopper outlet thicknesses ($D = 3$, 4, 5 and 8 mm) and for a fixed particle size $\bar{d}_p = 363\,\mu$m.

the particle group effect. This results in a lower particle acceleration and a smaller particle vertical separation at a given downstream location, thereby leading to a faster reduction of the rising rate in T for a smaller D. Nevertheless, the transmittance of a curtain with a larger D does not exceed that for a smaller D at a given downstream location. For example, $T = 0.66$ at $x = 900$ mm for $D = 3$ mm, which is some six times greater than $T = 0.11$ for $D = 8$ mm at the same location. This is because an increase in D also increases the number of particles at any given falling distance, which decreases T. Noting also that, according to the Beverloo equation the mass flow rate through the hopper (per unit width) scales with $D^{1.5}$, from (3.8). That is, $\bar{\theta}_0\ \rho_p\ \forall_p\ \bar{V}_0 \propto D^{0.5}$. For any given particle size, this implies that an increase in D, causes an increase in the initial particle velocity, and/or the initial particle concentration at the exit. The latter results in a decrease in transmittance in the near field, as measured in figure 15. A complete summary of measured curtain thickness and transmittance, along with details of the hopper geometry, is provided in the Supplementary Material available at https://doi.org/10.1017/jfm.2024.896.

4.4. *Insights into curtain evolution from analytical models*

Figure 19 presents a comparison of the measured axial evolution of a particle curtain transmittance together with that estimated from the Beer–Lambert model (3.9), for both the zero-drag (3.2) and Stokes-drag (3.4) models. As noted in § 3, these integrated models represent two extreme scenarios, which were developed to support the interpretation of the measured results, most notably, the axial evolution of the particle dynamics and its correlation with curtain transmittance. The results are shown for three different values of particle sizes (i.e. 163, 257 and 500 μm) and a single hopper outlet thickness of $D = 5$ mm. It can be seen that the transmittance calculated with the zero-drag model is always higher than that calculated with the Stokes-drag model. This is consistent with the understanding that the axial particle acceleration is greater for the case with no drag, leading to a greater axial separation between particles, and a higher void fraction. It can also be seen that the difference between the inferred transmittance profile for the Stokes-drag and the

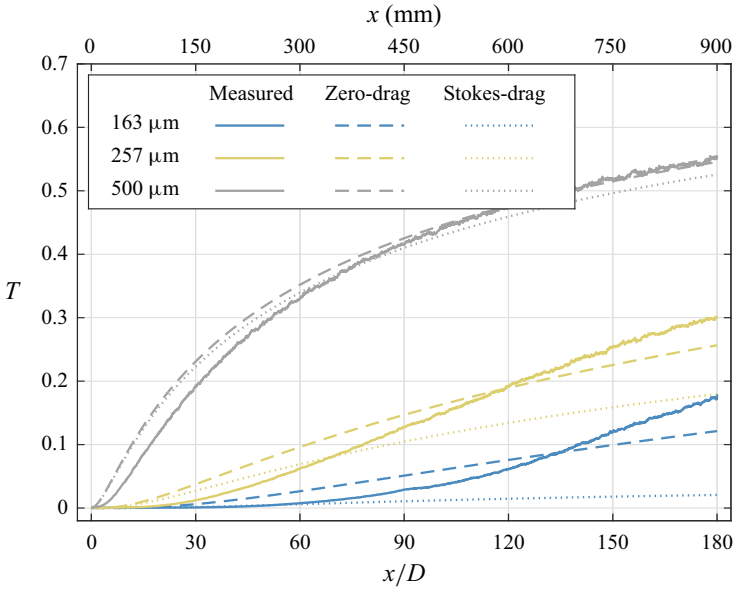

Figure 19. Comparison of the measured and modelled axial variation of transmittance for a particle curtain issuing from a hopper with different particle sizes ($\bar{d}_p = 163$, 257 and 500 μm) and a fixed hopper outlet thickness of $D = 5$ mm. The figure includes the transmittance calculated using two models, namely the zero-drag model (§ 3.1) and the Stokes-drag model (§ 3.2).

zero-drag models decreases with an increase in particle diameter. This can be explained by the drag force per unit weight of a particle decreasing with an increase in $\bar{d}_p$. That is, the influence of air drag decreases with an increase in $\bar{d}_p$. It can also be seen that both models tend to over-predict the transmittance in the near field and under-predict it at the end of the measured region in the intermediate field, particularly for the smallest particles. This is consistent with the particle dynamics in the near field being controlled by non-aerodynamic mechanisms of particle–particle interactions, as expected for a flow that originates in the granular flow regime. This granular regime decreases particle acceleration even beyond that for the Stokes regime. Furthermore, the measured transmittance at the end of the measurement region is greater than predicted with the zero-drag model, particularly for the smallest particles. This either implies that the particles accelerate faster than those with zero drag, which is implausible, or that the assumptions inherent in the current transmittance model, such as the assumption that particle scattering, particle shadowing and multiple scattering effects are negligible, and that the particle number density and velocity across the curtain at any given falling distance is uniform, begin to break down. Nevertheless, the comparison between different scenarios and associated mechanisms revealed herein also indicates that the particle dynamics predicted through the use of the Beverloo equation in these models is reasonable and consistent, thereby proving its validity in scaling assessments of flows as discussed for figure 5.

It can also be seen from figure 19 that the zero-drag model predicts the measured transmittance quite well for the largest particle size, consistent with the analysis of Sedaghatizadeh *et al.* (2022). This indicates that these larger particles approximate particles with zero drag, which is attributed to the decrease in drag per unit volume for larger $\bar{d}_p$ and the group effect whereby leading particles shield the upstream particles from

the effects of the surrounding fluid, causing them to fall faster than if they were in a quiescent, unperturbed, environment.

Given that the calculated curtain transmittance from the zero-drag model matches the experimental data more closely than the Stoke-drag model, but demonstrated with cases comprising only three particle sizes and one hopper outlet thickness, it would be insightful to expand the range of cases to fully examine its dimensionless correlations between all particle sizes and all hopper outlet thicknesses. In addition, it is also important to understand that the closest match for the largest particle size is primarily due to the effect of particle size rather than the hopper outlet thickness. To provide clear examinations, a special approach of rearranging the integrated analytical model into a linear relationship incorporating the Beverloo equation, the Beer–Lambert law and the zero-drag scenario, has been taken as follows.

The transmittance model can be further simplified by assuming the particles have zero drag. Combining (3.2) (particle velocity under the zero-drag assumption) and (3.9), we obtain

$$T(x) = \exp\left[-\frac{3\dot{M}_p}{2\rho_p d_p (U_0^2 + 2gx)^{0.5}}\right]. \tag{4.4}$$

If the particle-phase density (not to be confused with the particle material density, ρ_p) at the hopper exit is assumed to be the same as that within the hopper (i.e. equal to the particle bulk density ρ_b), then a calculation of the mass flow rate through the hopper exit results in a particle initial velocity of $U_0 = (\dot{M}_p)/(\rho_b D)$. Now, utilising the Beverloo equation (4.1), and assuming that the d_p/D term is small, (4.4) becomes

$$\frac{C_1^2}{2}\left[\frac{1}{(\kappa \ln T(x))^2} - 1\right] = \frac{x}{D}, \tag{4.5}$$

where $\kappa = 2/3(\rho_p/\rho_b)(d_p/D)$ is a dimensionless ratio, accounting for density and size differences.

The experimental results of $C_1^2[1/(\kappa \ln T(x))^2 - 1]/2$ as a function of x/D are presented in figure 20, with panel (a) presenting results for a single hopper outlet thickness of $D = 5$ mm with seven different $\bar{d}_p$ and panel (b) presenting results for a single particle size $\bar{d}_p = 500\,\mu$m with different D. The black dashed line in figure 20(a) represents a linear relationship with a gradient of unity, as expected from (4.5). It can be seen that the profile for the largest particle size, $\bar{d}_p = 500\,\mu$m, matches the linear function quite closely, with the data departing from this line with a reduction in $\bar{d}_p$, particularly for $\bar{d}_p \leq 363\,\mu$m. The departure of the experimental data from the trends predicted with (4.5) for sufficiently small particles, as shown in figure 20(a), is attributed to the simplifications and assumptions invoked in the derivation of (4.5), particularly in the assumption that the particle drag is zero. The relatively closely matched profile for $\bar{d}_p = 500\,\mu$m can also be seen in figure 20(b) for other D, although some departure happens for $D = 3$ mm, potentially due to an increasing effect of non-zero drag caused by particle dispersion, which is consistent with the analysis of K_{int} in figure 12(b). That is, this analytical model provides a reasonable estimate of transmittance for sufficiently large particles ($\bar{d}_p \geq 399\,\mu$m), with the hopper thickness as a secondary effect, notwithstanding the slight under-prediction in the near field and over-prediction in the intermediate field.

In addition, it can also be seen that this method of normalisation gives a pretty good collapse of the measurements of the curtains with smaller particles, but onto a different curve, as described by the function inserted in figure 20(a), which applies for the regime

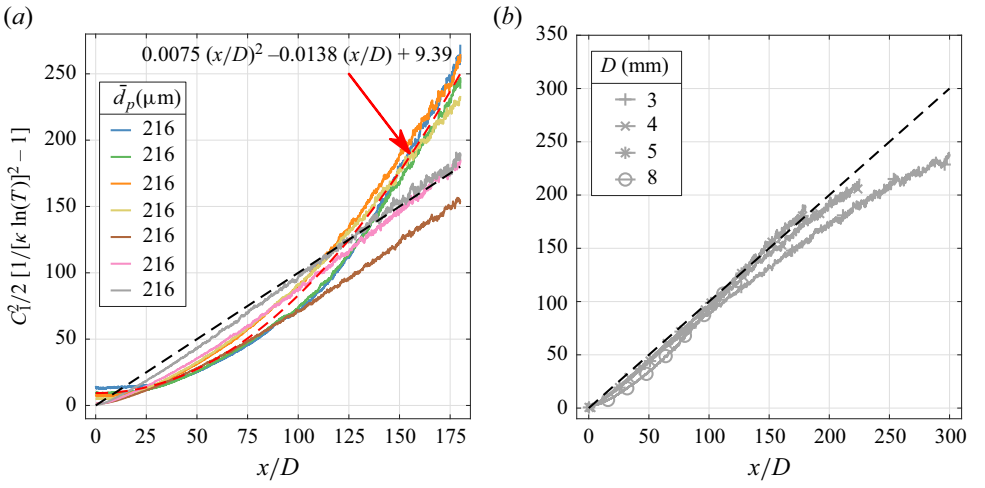

Figure 20. The measured particle curtain transmittance (T), normalised based on (4.5), as a function of normalised falling distance (x/D) for (a) seven different particle sizes with the hopper $D = 5$ mm and (b) four different hopper outlet thicknesses with the particle size $\bar{d}_p = 500\,\mu$m. The black dashed line represents a gradient of unity, while the red dashed line indicates a different asymptotic curve fitted based on profiles of $\bar{d}_p = 163$–$257\,\mu$m using a quadratic function which is included in the inset equation.

where particle drag is significant. These data have a lower slope than unity function in the near field and a higher slope for $x/D > 110$. That the data collapse with this normalisation highlights the importance of initial curtain momentum in both regimes, since the normalisation utilising the Beverloo equation accounts for the particle mass flow rate and initial velocity. That the data collapse onto two curves demonstrates that curtains can be characterised broadly into the regimes in which aerodynamic drag is overall dominant or weak throughout these near and intermediate regions.

4.5. *Summary of characterised flow regions for free-falling particle curtain flows*

Figure 21 presents a schematic diagram of the key features of, and mechanisms for, the evolution of a free-falling particle curtain from a rectangular orifice at the base of a hopper. The 'hopper-flow dominant regime' identified by Sedaghatizadeh *et al.* (2022) has been theoretically expanded into two regions to yield a total of four regions in the axial direction with the additional information also provided on the third region, i.e. 'the similarity regime', from the present new data. At the lateral plane, new information of an extra region of dispersed particles in addition to the curtain core region has also been provided. Overall, the curtain has been characterised into regions in both vertical and horizontal directions as follows:

(i) The near-field expansion region: this is characterised by rapid spreading immediately below the hopper exit and is deduced to be induced by particle collisions that result from the gradients in particle velocity close to the edge of the curtain due to wall friction within the hopper.

(ii) The neck zone: this zone is typically downstream from the near-field expansion region, and is characterised by a necking process whereby the curtain thickness decreases with axial distance. This process is attributed to the influence of particle acceleration due to gravity, which induces a low-pressure region along the axis of the curtain.

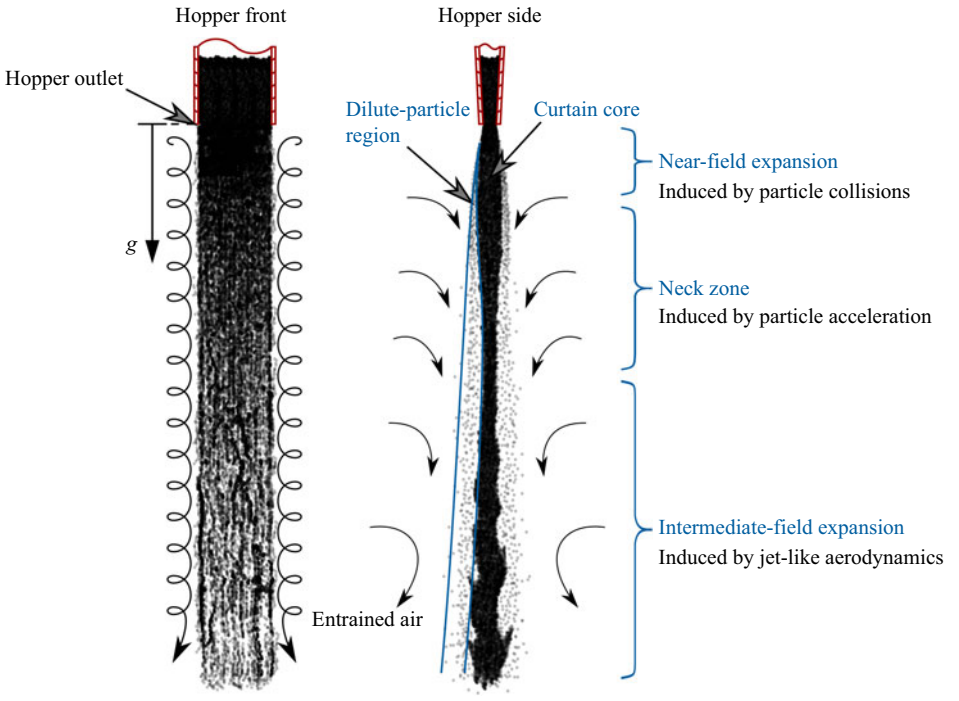

Figure 21. Schematic diagram with cartoon of key features of, and deduced mechanism for, a free-falling particle curtain discharged from a hopper with a rectangular outlet.

(iii) The intermediate-field expansion region: this region is characterised by an expansion of the curtain thickness downstream from the curtain neck (i.e. the point where the curtain thickness approaches a local minimum) due to the entrainment of air into the curtain. This region is characterised by large-scale flow unsteadiness that is deduced to be induced by a jet-like aerodynamics. The particle flow in this region transitions from the hopper-flow dominant condition to the regime where particles are approaching terminal velocity so that it theoretically matches with the similarity regime as identified by Sedaghatizadeh *et al.* (2022).

(iv) The terminal velocity region: this 'far-field' region, while not investigated directly here, has been shown previously to correspond to the region in which particles decelerate towards the terminal velocity of an individual particle (Sedaghatizadeh *et al.* 2022).

(v) The curtain core: this central region of the curtain is densely loaded with particles, so that their wakes are interconnected to generate a strong particle group effect that reduces the bulk fluid drag. This region also provides a foundation for the axial regions defined above.

(vi) The dilute-particle region: this region laterally surrounds the curtain core, expanding continuously downstream from the near-exit region. It results from the initial particle lateral momentum, which is generated in turn by particle–wall and particle–particle interactions at the exit.

In the near-field expansion region, particles were found to expand immediately downstream from the exit plane with an expansion gradient of $0.0796 \leq K_{near} \leq 0.1703$, corresponding to an expansion half-angle of $2.3^\circ \leq \alpha \leq 4.8^\circ$. The near-field expansion

rate increases with hopper outlet thickness and, weakly, with particle size. At the end of the near-field expansion region, a local peak in the curtain thickness was typically observed, with a local maximum curtain thickness falling in the range of $1.61 \leq \Delta_{0.5,pk}/D \leq 2.54$. The relative axial location of the local peak, $4.96 \leq x_{pk}/D \leq 26.29$, was found to increase monotonically with particle size. Particle collisions were deduced to be the primary source of the particle lateral momentum and to be responsible for the near-field expansion, from which particle–hopper interactions can be expected to have a dominant influence on the flow behaviour. This needs to be further verified by measuring the particle velocity and the inter-particle collisions at the near-exit region.

In the neck zone, just downstream from the local maximum in the curtain thickness (i.e. at the downstream end of the near-field expansion region), the particle curtain was found to decrease in thickness, leading to a local 'trough' feature with the curtain thickness narrowing down to $0.78 \leq \Delta_{0.5,tr}/D \leq 2.53$. The magnitude of $\Delta_{0.5,tr}/D$ was found to increase with $\bar{d}_p/D$, while the difference in the magnitude between $\Delta_{0.5,pk}/D$ and $\Delta_{0.5,tr}/D$ was found to reduce with increasing $\bar{d}_p/D$. As a result, no obvious peak or trough feature was identified for the case of $\bar{d}_p = 500\,\mu\text{m}$ and $D = 3\,\text{mm}$. Interestingly, the relative location of the local minimum in curtain thickness, $42.35 \leq x_{tr}/D \leq 73.72$, was found to form an 'arch'-shaped curve with the maximum value of x_{tr}/D occurring for $\bar{d}_p/D \approx 0.05$. The above findings highlight the complex nature of the flow in the neck zone, where the dominant influence is plausibly attributed to the momentum balance between the particle inertia (initial momentum) which drives the particle spreading continuously from the near-field expansion and the drag of the entrained air on the particles towards the curtain core due to the pressure gradients generated by particle acceleration. That is, particle inertia dominates the flow behaviour for the normalised particle size range of $\bar{d}_p/D > 0.05$, while the effect of surrounding fluid generated by the high particle mass flow rate is the key influence in the cases using a relatively large hopper outlet thickness, i.e. $\bar{d}_p/D < 0.05$. Further insight would require additional measurements of the particle velocity and the air velocity in the surrounding region close to the particles.

In the intermediate-field expansion region, downstream from the local minimum in curtain thickness (i.e. the neck), particles were found to expand with axial distance. In this region, large-scale flow unsteadiness that spans the entire width of the curtain was observed. The rate of expansion in the intermediate field, $0.00347 \leq K_{int} \leq 0.0226$, is approximately one order of magnitude smaller than that in the near field. Furthermore, the trend of the dependence of the expansion rate in the intermediate field on particle size and hopper outlet thickness was found to be opposite to that in the near field, with K_{int} decreasing as $\bar{d}_p$ and D are increased. This is consistent with the controlling mechanism being driven by aerodynamic drag, as proposed previously (Sedaghatizadeh *et al.* 2022). In addition, the influence of particle inertia increases with D due to both the greater particle axial momentum and particle group effect reducing the fluid drag, which leads to a decrease of the K_{int}.

The radial particle distribution of the dilute region was found to have a rapid initial expansion comparable to that of the near-field expansion. This suggests that both are caused by similar mechanisms of particle–particle and particle–wall interactions. However, downstream from there, the dilute-particle region expands continuously, so that it does not exhibit the necking, which implies that it is not influenced by the transverse pressure gradients within the core that are induced by particle acceleration. The lateral expansion of the dilute-particle region continues to increase with a decrease in $\bar{d}_p$ through the intermediate field, which suggests the fluid drag controls its entire lateral evolution.

5. Conclusions

The first of the three regimes identified by Sedaghatizadeh *et al.* (2022) to characterise the evolution of free-falling particle curtains released from a rectangular orifice of a hopper has been subdivided into the near-field expansion and the neck zone to yield a total of four axial regions (described above). In addition, the presence of the dilute-particle region that surrounds the entire curtain in the lateral direction has been identified for the first time. New insights have also been provided for each of these four axial regions and the new lateral region from systematic measurements of four different hopper outlet thickness ($D =$ 3, 4, 5 and 8 mm), and seven particle sizes ($\bar{d}_p =$ 163, 192, 216, 257, 363, 399 and 500 μm). The dominant mechanism controlling particle spreading in the near-field expansion region is deduced to be that of particle collisions, which are caused by velocity gradients at the edge of the curtain that result, in turn, from wall friction within the hopper, while the third intermediate-field expansion region is driven by aerodynamic drag (particle–air). The neck zone of the curtain is formed as a result of momentum balance between particle inertia, which scales with particle size, and pressure gradient that is driven by particle acceleration due to gravity, which is influenced mostly by hopper outlet thickness.

For a given set of conditions, the axial evolution of particle curtain transmittance, T, was found to be influenced mostly by particle acceleration in the vertical direction, which controls the average particle number density at a given lateral plane. However, the dependence of this evolution on particle diameter and curtain thickness is complex and nonlinear. The axial rise in near-field transmittance increases with the particle diameter due both to the increase in axial velocity and the decrease in particle cross-sectional area per unit volume. This combined effect increases the vertical spacing between particles and enhances the chances of light transmitting through the curtain. However, this trend also continues for the neck zone and intermediate-field region where the curtain thickness evolves differently from the near field. That is, T increases with $\bar{d}_p$ for all regions and cases we studied. In addition, the increase in transmittance was found to scale with the product of Froude number based on drag-free particle terminal velocity and x/D. These dependences are consistent with the evolution of T being dominated by the axial spacing between particles, which is controlled by gravity. A collapse of all T profiles onto two curves when normalised using the Beverloo equation (figure 20), which characterises the initial velocity, demonstrates that curtains can be characterised broadly into the regimes in which aerodynamic drag is overall dominant or weak throughout these near and intermediate regimes.

The generation of the dilute-particle region, i.e. a region with particles at a low volume fraction around the denser core of the particle curtain, originates from the near-field expansion. That is, these particles originate from particle collisions generated by the non-uniform velocity distribution at the exit of the hopper, and, in turn, from friction-induced gradients at the walls of the hopper. Some of these particles are dispersed beyond the range where the particle-acceleration-induced pressure gradient can draw them back into the curtain, so that the layer persists throughout the evolution of the curtain, retaining its thickness for at least $40D$ before becoming influenced by aerodynamic drag. These particles can be expected to be influenced by secondary flows within practical devices such as solar thermal falling particle receivers, generating a potential source for emission of fine particles. Importantly, this dispersion mechanism induces a lateral velocity component to the particles, which does not therefore influence the evolution of transmittance significantly. In addition to the deduced role of wall friction in generating this dispersion mechanism, it suggests that the hopper's shape may also induce lateral movement and influence this dilute-particle region. Furthermore, the significance of this

layer increases with particle diameter, since larger particles have greater lateral inertia and are less influenced by the aerodynamic drag that acts to entrain particles into the curtain.

Particle curtains with larger $\bar{d}_p$ were found to more closely approximate the zero-drag idealisation (i.e. acceleration in a vacuum) with greater downstream distances, while the zero-drag model under-predicted the curtain transmittance for smaller $\bar{d}_p$. This is attributed, in part, to the increased role of particle–particle light interactions, which were ignored in the model. The relatively good predictions from the zero-drag model also imply that the volumetric loading is sufficiently good to account for the role of the particle 'group' effect, in which the drag of particles is reduced by wake interactions. This mechanism acts to reduce the particle dispersion and to increase the axial spacing between particles.

The measured instantaneous distribution of particles becomes highly non-uniform at a sufficient axial distance, with strong variations both spatially and temporally, caused by filament- or rope- like particle clusters aligned with the direction of gravity. The aerodynamic 'clustering' phenomenon of particles induces spatial variations in particle number density, which further influence the instantaneous non-uniformity in transmittance. These can be expected to introduce challenges in running and in predicting industrial systems employing falling particles, such as FPRs. Despite a few pioneering studies on this topic, more direct measurements of the dynamics of clustering structures are still needed to improve the understanding of the relationship between their formation and subsequent evolution.

Supplementary material. Supplementary material is available at https://doi.org/10.1017/jfm.2024.896.

Funding. The authors gratefully acknowledge the internationally financial contributions from the U.S. Department of Energy, Sandia National Laboratories through the Gen 3 Particle Pilot Plant (G3P3): Integrated High-Temperature Particle Receiver System for CSP (1697-1503) and the Australian government through the Australian Research Council (Discovery Grant DP180102045) and the Australian Renewable Energy Agency (Grant 2015/RND054).

Declaration of interests. The authors report no conflict of interest.

Author ORCIDs.
Xiaopeng Bi https://orcid.org/0000-0001-9084-7325;
Timothy C.W. Lau https://orcid.org/0000-0003-1851-706X;
Zhiwei Sun https://orcid.org/0000-0001-7899-9676;
Graham J. Nathan https://orcid.org/0000-0002-6922-848X.

References

Abdul-Wahab, S.A. 2006 Impact of fugitive dust emissions from cement plants on nearby communities. *Ecol. Model.* **195**, 338–348.

Amarouchene, Y., Boudet, J.F. & Kellay, H. 2008 Capillarylike fluctuations at the interface of falling granular jets. *Phys. Rev. Lett.* **100**, 218001.

Anand, A., Curtis, J.S., Wassgren, C.R., Hancock, B.C. & Ketterhagen, W.R. 2008 Predicting discharge dynamics from a rectangular hopper using the discrete element method (dem). *Chem. Engng Sci.* **63**, 5821–5830.

Ang, D., Chinnici, A., Tian, Z.F., Saw, W.L. & Nathan, G.J. 2022 Influence of particle loading, Froude and Stokes number on the global thermal performance of a vortex-based solar particle receiver. *Renew. Energy* **184**, 201–214.

Ansart, R., De Ryck, A., Dodds, J.A., Roudet, M., Fabre, D. & Charru, F. 2009 Dust emission by powder handling: comparison between numerical analysis and experimental results. *Powder Technol.* **190**, 274–281.

Ansart, R., Letourneau, J.J., De Ryck, A. & Dodds, J.A. 2011 Dust emission by powder handling: influence of the hopper outlet on the dust plume. *Powder Technol.* **212**, 418–424.

Bagepalli, M.V., Yarrington, J.D., Schrader, A.J., Zhang, Z.M., Ranjan, D. & Loutzenhiser, P.G. 2020 Measurement of flow properties coupled to experimental and numerical analyses of dense, granular flows for solar thermal energy storage. *Sol. Energy* **207**, 77–90.

Balachandar, S. & Eaton, J.K. 2010 Turbulent dispersed multiphase flow. *Annu. Rev. Fluid Mech.* **42**, 111–133.

Beverloo, W.A., Leniger, H.A. & Van de Velde, J. 1961 The flow of granular solids through orifices. *Chem. Engng Sci.* **15**, 260–269.

Brown, R.L. 1961 Minimum energy theorem for flow of dry granules through apertures. *Nature* **191**, 458–461.

Capecelatro, J., Desjardins, O. & Fox, R.O. 2015 On fluid–particle dynamics in fully developed cluster-induced turbulence. *J. Fluid Mech.* **780**, 578–635.

Carbo Ceramic, Inc. 2022 Techanical data sheet. https://carboceramics.com/getmedia/f3f7794b-9cd4-4a8f-8184-93eb75f5bddd/CARBOBEAD-Technical-Data-Sheet-1001_317v5.pdf?ext=.pdf.

Chu, K.W., Wang, Y., Zheng, Q.J., Yu, A.B. & Pan, R.H. 2020 Cfd-dem study of air entrainment in falling particle plumes. *Powder Technol.* **361**, 836–848.

Cleary, P.W. & Sawley, M.L. 2002 Dem modelling of industrial granular flows: 3D case studies and the effect of particle shape on hopper discharge. *Appl. Math. Model.* **26**, 89–111.

Cooper, P. & Arnold, P. 1995 Air entrainment and dust generation from a falling stream of bulk material. *Kona Powder Part.* J **13**, 125–134.

Datta, A., Mishra, B.K., Das, S.P. & Sahu, A. 2008 A dem analysis of flow characteristics of noncohesive particles in hopper. *Mater. Manuf. Process.* **23**, 195–202.

Deo, R.C., Mi, J. & Nathan, G.J. 2007 The influence of nozzle aspect ratio on plane jets. *Exp. Therm. Fluid Sci.* **31**, 825–838.

Eaton, J.K. & Fessler, J.R. 1994 Preferential concentration of particles by turbulence. *Intl J. Multiphase Flow* **20**, 169–209.

Eckhoff, R.K. 2005 Current status and expected future trends in dust explosion research. *J. Loss Prev. Process. Ind.* **18**, 225–237.

Esmaili, A.A., Donohue, T.J., Wheeler, C.A., McBride, W.M. & Roberts, A.W. 2015 On the analysis of a coarse particle free falling material stream. *Intl J. Miner. Process.* **142**, 82–90.

Evans, G., Houf, W., Greif, R. & Crowe, C. 1987 Gas-particle flow within a high temperature solar cavity receiver including radiation heat transfer. *J. Sol. Energy Engng* **109**, 134–142.

Fabiano, B., Currò, F., Reverberi, A.P. & Palazzi, E. 2014 Coal dust emissions: from environmental control to risk minimization by underground transport. An applicative case-study. *Process. Saf. Environ.* **92**, 150–159.

Falcone, P.K., Noring, J.E. & Hruby, J.M. 1985 Assessment of a solid particle receiver for a high temperature solar central receiver system. *Tech. Rep.* Sandia National Lab.(SNL-CA).

Fitzpatrick, J.J. & Ahrné, L. 2005 Food powder handling and processing: industry problems, knowledge barriers and research opportunities. *Chem. Engng Process.* **44**, 209–214.

Gobereit, B., Amsbeck, L., Happich, C. & Schmücker, M. 2020 Assessment and improvement of optical properties of particles for solid particle receiver. *Sol. Energy* **199**, 844–851.

Hardalupas, Y., Taylor, A.M.K.P. & Whitelaw, J.H. 1989 Velocity and particle-flux characteristics of turbulent particle-laden jets. *Proc. R. Soc. Lond.* A **426**, 31–78.

Ho, C., Christian, J., Gill, D., Moya, A., Jeter, S., Abdel-Khalik, S., Sadowski, D., Siegel, N., Al-Ansary, H. & Amsbeck, L. 2014 Technology advancements for next generation falling particle receivers. *Energy Procedia* **49**, 398–407.

Ho, C.K. 2016 A review of high-temperature particle receivers for concentrating solar power. *Appl. Therm. Engng* **109**, 958–969.

Ho, C.K. 2017 Advances in central receivers for concentrating solar applications. *Sol. Energy* **152**, 38–56.

Ho, C.K., Christian, J.M., Romano, D., Yellowhair, J., Siegel, N., Savoldi, L. & Zanino, R. 2017 Characterization of particle flow in a free-falling solar particle receiver. *J. Sol. Energy Engng* **139**, 021011.

Ho, C.K., Christian, J.M., Yellowhair, J.E., Armijo, K., Kolb, W.J., Jeter, S., Golob, M. & Nguyen, C. 2019 On-sun performance evaluation of alternative high-temperature falling particle receiver designs. *J. Sol. Energy Engng* **141**, 011009.

Ho, C.K., Christian, J.M., Yellowhair, J., Siegel, N., Jeter, S., Golob, M., Abdel-Khalik, S.I., Nguyen, C. & Al-Ansary, H. 2016 On-sun testing of an advanced falling particle receiver system. *AIP Conf. Proc.* **1734**, 030022.

Ho, C.K. & Iverson, B.D. 2014 Review of high-temperature central receiver designs for concentrating solar power. *Renew. Sustain. Energy Rev.* **29**, 835–846.

HRUBY, J., STEEPER, R., EVANS, G. & CROWE, C. 1988 An experimental and numerical study of flow and convective heat transfer in a freely falling curtain of particles. *J. Fluids Eng.* **110**, 172–181.

HRUBY, J.M. 1986 Technical feasibility study of a solid particle solar central receiver for high temperature applications. *Tech. Rep.* Sandia National Labs.

JANDA, A., ZURIGUEL, I. & MAZA, D. 2012 Flow rate of particles through apertures obtained from self-similar density and velocity profiles. *Phys. Rev. Lett.* **108**, 248001.

JEONG, S.Y., CHEN, C., RANJAN, D., LOUTZENHISER, P.G. & ZHANG, Z.M. 2021 Measurements of scattering and absorption properties of submillimeter bauxite and silica particles. *J. Quant. Spectrosc. Radiat. Transfer* **276**, 107923.

JOHNSON, P.C., NOTT, P. & JACKSON, R. 1990 Frictional–collisional equations of motion for participate flows and their application to chutes. *J. Fluid Mech.* **210**, 501–535.

KHALSA, S.S.S. & HO, C.K. 2011 Radiation boundary conditions for computational fluid dynamics models of high-temperature cavity receivers. *J. Sol. Energy Engng* **133**, 031020.

KIM, K., MOUJAES, S.F. & KOLB, G.J. 2010 Experimental and simulation study on wind affecting particle flow in a solar receiver. *Sol. Energy* **84**, 263–270.

KIM, K., SIEGEL, N., KOLB, G., RANGASWAMY, V. & MOUJAES, S.F. 2009 A study of solid particle flow characterization in solar particle receiver. *Sol. Energy* **83**, 1784–1793.

KNOTT, R.C., SADOWSKI, D.L., JETER, S.M., ABDEL-KHALIK, S.I., AL-ANSARY, H.A. & EL-LEATHY, A. 2014 High temperature durability of solid particles for use in particle heating concentrator solar power systems. In *Energy Sustainability*, vol. 45868, p. V001T02A041. American Society of Mechanical Engineers.

KUMAR, A., KIM, J.S. & LIPIŃSKI, W. 2018 Radiation absorption in a particle curtain exposed to direct high-flux solar irradiation. *J. Sol. Energy Engng* **140**, 061007.

KUMAR, A., LIPIŃSKI, W. & KIM, J.S. 2020 Numerical modelling of radiation absorption in a novel multi-stage free-falling particle receiver. *Intl J. Heat Mass Transfer* **146**, 118821.

LAU, T.C.W., FRANK, J.H. & NATHAN, G.J. 2019 Resolving the three-dimensional structure of particles that are aerodynamically clustered by a turbulent flow. *Phys. Fluids* **31**, 071702.

LAU, T.C.W. & NATHAN, G.J. 2014 Influence of Stokes number on the velocity and concentration distributions in particle-laden jets. *J. Fluid Mech.* **757**, 432–457.

LAU, T.C.W. & NATHAN, G.J. 2016 The effect of Stokes number on particle velocity and concentration distributions in a well-characterised, turbulent, co-flowing two-phase jet. *J. Fluid Mech.* **809**, 72–110.

LAU, T.C.W. & NATHAN, G.J. 2017 A method for identifying and characterising particle clusters in a two-phase turbulent jet. *Intl J. Multiphase Flow* **88**, 191–204.

LEWIS, E.W., LAU, T.C.W., SUN, Z., ALWAHABI, Z.T. & NATHAN, G.J. 2021 Insights from a new method providing single-shot, planar measurement of gas-phase temperature in particle-laden flows under high-flux radiation. *Exp. Fluids* **62**, 1–17.

LEWIS, E.W., LAU, T.C.W., SUN, Z., ALWAHABI, Z.T. & NATHAN, G.J. 2022 The effect of particle size and volumetric loading on the gas temperature distributions in a particle-laden flow heated with high-flux radiation. *Intl J. Heat Mass Transfer* **182**, 122041.

LI, X., WANG, Q., LIU, Q. & HU, Y. 2016 Developments in studies of air entrained by falling bulk materials. *Powder Technol.* **291**, 159–169.

LIU, Z. 2003 Air entrainment in free falling bulk materials. PhD thesis, University of Wollongong.

LIU, Z., COOPER, P. & WYPYCH, P.W. 2007 Experimental investigation of air entrainment in free-falling particle plumes. *Particul. Sci. Technol.* **25**, 357–373.

LONGMIRE, E.K. & EATON, J.K. 1992 Structure of a particle-laden round jet. *J. Fluid Mech.* **236**, 217–257.

MANKOC, C., JANDA, A., AREVALO, R., PASTOR, J.M., ZURIGUEL, I., GARCIMARTÍN, A. & MAZA, D. 2007 The flow rate of granular materials through an orifice. *Granul. Matt.* **9**, 407–414.

MARTIN, J. & VITKO, J., JR. 1982 Ascuas: a solar central receiver utilizing a solid thermal carrier. *Tech. Rep.* Sandia National Lab.(SNL-CA).

MAXEY, M.R. 1987 The gravitational settling of aerosol particles in homogeneous turbulence and random flow fields. *J. Fluid Mech.* **174**, 441–465.

MI, J., NOBES, D.S. & NATHAN, G.J. 2001 Influence of jet exit conditions on the passive scalar field of an axisymmetric free jet. *J. Fluid Mech.* **432**, 91–125.

MILLS, B. & HO, C.K. 2019 Simulation and performance evaluation of on-sun particle receiver tests. *AIP Conf. Proc.* **2126**, 030036.

MILLS, B., SHAEFFER, R., HO, C.K. & YUE, L. 2019 Modeling the thermal performance of falling particle receivers subject to external wind. In *Energy Sustainability*, vol. 59094, p. V001T03A011. AIP Publishing.

MÖBIUS, M.E. 2006 Clustering instability in a freely falling granular jet. *Phys. Rev.* E **74**, 051304.

NEDDERMAN, R.M., TÜZÜN, U., SAVAGE, S.B. & HOULSBY, G.T. 1982 Flow of granular materials-I. Discharge rates from hoppers. *Chem. Engng Sci.* **37**, 1597–1609.

OGATA, K., FUNATSU, K. & TOMITA, Y. 2001 Experimental investigation of a free falling powder jet and the air entrainment. *Powder Technol.* **115**, 90–95.

PRADO, G., AMAROUCHENE, Y. & KELLAY, H. 2011 Experimental evidence of a Rayleigh-Plateau instability in free falling granular jets. *Phys. Rev. Lett.* **106**, 198001.

PRADO, G., AMAROUCHENE, Y. & KELLAY, H. 2013 Incompressible-compressible transition in falling granular jets. *Europhys. Lett.* **102**, 24006.

SEDAGHATIZADEH, N., ARJOMANDI, M., LAU, T. & NATHAN, G. 2022 The dominant underlying parameters controlling the dispersion of falling particle curtains. *Powder Technol.* **402**, 117343.

SIEGEL, N., KOLB, G., KIM, K., RANGASWAMY, V. & MOUJAES, S. 2007 Solid particle receiver flow characerization studies. In *Energy Sustainability*, vol. 47977, pp. 877–883. American Society of Mechanical Engineers.

SIEGEL, N.P., GROSS, M.D. & COURY, R. 2015 The development of direct absorption and storage media for falling particle solar central receivers. *J. Sol. Energy Engng* **137**, 041003.

SQUIRES, K.D. & EATON, J.K. 1991 Preferential concentration of particles by turbulence. *Phys. Fluids* A **3**, 1169–1178.

SUN, H., LI, A., LONG, J., WU, J., ZHANG, W. & ZHANG, J. 2020*a* Experimental study on the characteristics of entrained air during the particle flow fall process. *Powder Technol.* **374**, 421–429.

SUN, H., LI, A., WU, J. & ZHANG, J. 2020*b* Particle flow fall process: a systematic study of entrained air under unconfined and semi-confined fall conditions. *Granul. Matt.* **22**, 1–11.

UCHIYAMA, T. 2004 Numerical analysis of particulate jet generated by free falling particles. *Powder Technol.* **145**, 123–130.

WANG, M.K., YANG, G.H., ZHANG, S., CAI, H.J., LIN, P., CHEN, L.W. & YANG, L. 2020 A numerical study of dynamics in thin hopper flow and granular jet. *Chin. Phys.* B **29**, 048102.

WANG, Y., REN, X., ZHAO, J., CHU, Z., CAO, Y., YANG, Y., DUAN, M., FAN, H. & QU, X. 2016 Experimental study of flow regimes and dust emission in a free falling particle stream. *Powder Technol.* **292**, 14–22.

WARDJIMAN, C., LEE, A., SHEEHAN, M. & RHODES, M. 2009 Shape of a particle curtain falling in stagnant air. *Powder Technol.* **192**, 384–388.

WYPYCH, P., COOK, D. & COOPER, P. 2005 Controlling dust emissions and explosion hazards in powder handling plants. *Chem. Engng Process.* **44**, 323–326.